Dual-hit strategy for therapeutic targeting of pancreatic cancer in patient-derived xenograft tumors

Tista Roy Chaudhuri [1*], Qingxiang Lin [2], Ewa K. Stachowiak [3], Spencer R. Rosario [4], Joseph A. Spernyak [2], Wen Wee Ma [5], Michal K. Stachowiak [3], Michelle K. Greene [6], Gerard P. Quinn [6], Simon S. McDade [6], Martin Clynes[7], Christopher J. Scott [6] and Robert M. Straubinger [1,3 *]

[1] Department of Pharmaceutical Sciences,
University at Buffalo, State University of New York, Buffalo, NY 14214

[2] Department of Cell Stress Biology
Roswell Park Comprehensive Cancer Center, Buffalo, NY 14263

[3] Department of Pathology and Anatomical Sciences,
University at Buffalo, State University of New York, Buffalo, NY 14214

[4] Department of Bioinformatics and Biostatistics
Roswell Park Comprehensive Cancer Center, Buffalo, NY 14263

[5] Department of Hematology and Oncology
Taussig Cancer Institute, Cleveland Clinic
Cleveland, OH, 44106

[6] The Patrick G Johnston Centre for Cancer Research, School of Medicine, Dentistry and Biomedical Sciences, Queen's University Belfast, Belfast BT9 7AE, UK

[7] The National Institute for Cellular Biotechnology, Dublin City University, Glasnevin 9, Dublin, Ireland

Running title: SHHi+FGFRi enhances PDAC tumor permeability and reverses EMT

*** Co-Corresponding Authors**. TRC: tr22@buffalo.edu; RMS: rms@buffalo.edu

Contact Corresponding Author:
Robert M. Straubinger, Ph.D.
Department of Pharmaceutical Sciences
University at Buffalo, State University of New York
Buffalo, N.Y., U.S.A. 14214

Email: *rms@Buffalo.edu*

Telephone: (716) 645-2844

FAX: (716) 829-6569

Tista Roy Chaudhuri
Department of Pharmaceutical Sciences,
University at Buffalo, State University of New York
Buffalo, N.Y., U.S.A. 14214
tr22@buffalo.edu
716 645 4814

Abbreviations

ADC	Apparent Diffusion Coefficient
rADC	Apparent Diffusion Coefficient relative to baseline
CAF	Carcinoma-associated fibroblasts
DiIC18(5)-DS	Dioctadecyl-3,3,3',3'-tetramethylindocarbocyanine disulfonate
DCE-MRI	Dynamic contrast enhanced Magnetic Resonance Imaging
DW-MRI	Diffusion-weighted Magnetic Resonance Imaging
EMT	Epithelial-to-mesenchymal transition
FGFRi	Small molecule tyrosine kinase inhibitor specific to FGF receptors 1,2,3
FDR	False discovery rate
HH	Hedgehog signaling pathway
Ihh	Indian hedgehog ligand
INFS	Integrative nuclear FGFR1 signaling
nuFGFR1	Nuclear-localizing fragment of FGFR1
Shh	Sonic hedgehog ligand
SHG	Second Harmonic Generation
SHHi	SMO inhibitor of hedgehog signaling
SSL	Sterically stabilized liposomes
SSL-DiI	Sterically stabilized liposomes labeled with fluorescent probe DiIC18(5)-DS

Conflict of interest: The authors declare no competing interests.

Keywords: *Pancreatic cancer; Nanoparticle drug delivery; SMO hedgehog signaling inhibitor; Diffusion-weighted MRI; Apparent diffusion coefficient; Nuclear FGFR1; Stromal targeting; Magnetic resonance imaging; Tumor priming.*

Translational Relevance

Pancreatic adenocarcinoma (PDAC) is a dismal disease, and progress in extending survival is incremental. Low vascular perfusion and permeability resulting from desmoplasia are key contributors to treatment resistance. Stroma-targeting strategies employing small-molecule SMO inhibitors of hedgehog signaling (SHHi) to prime tumors for enhanced delivery of chemotherapy faltered clinically for lack of a detailed understanding of underlying molecular mechanisms. We found that SHHi induction of vascular permeability/perfusion varies in efficacy within a panel of patient-derived xenografts, and that diffusion-weighted MR imaging identifies alterations in PDAC tumors that correlate with increased nanoparticle deposition, non-invasively predicting responders to SHHi-therapy. We also observed that SHHi treatment evokes epithelial-to-mesenchymal-transition (EMT) along with FGFR overexpression and signaling deregulation. Short-term dosing with FDA-approved FGFR inhibitors reversed SHHi-mediated EMT while maintaining elevated tumor vascular perfusion, permeability, and nanoparticle delivery. This promising dual-hit strategy is clinically feasible for enhancing PDAC tumor drug delivery while suppressing potentially deleterious EMT-related effects.

Abstract

Purpose: Paracrine activation of pro-fibrotic hedgehog (HH) signaling in pancreatic ductal adenocarcinoma (PDAC) results in stromal amplification that compromises tumor drug delivery, efficacy, and patient survival. Interdiction of HH-mediated tumor-stroma crosstalk with smoothened (SMO) inhibitors (SHHi) 'primes' PDAC patient-derived xenograft (PDX) tumors for increased drug delivery by transiently increasing vascular patency/permeability, and thereby macromolecule delivery. However, patient tumor isolates vary in their responsiveness, and responders show co-induction of epithelial-mesenchymal transition (EMT). We aimed to identify the signal derangements responsible for EMT induction and reverse them, and devise approaches to stratify SHHi-responsive tumors non-invasively based on clinically-quantifiable parameters.

Experimental design: Animals underwent diffusion-weighted magnetic resonance (DW-MR) imaging for measurement of intra-tumor diffusivity. In parallel, tissue-level deposition of nanoparticle probes was quantified as a marker of vascular permeability/perfusion. Transcriptomic and bioinformatic analysis was employed to investigate SHHi-induced gene reprogramming and identify key 'nodes' responsible for EMT induction.

Results: multiple patient tumor isolates responded to short-term SHH inhibitor exposure with increased vascular patency and permeability, with proportionate increases in tumor diffusivity. Non-responding PDXs did not. SHHi-treated tumors showed elevated FGF drive and distinctly higher nuclear localization of fibroblast growth factor receptor (FGFR1) in EMT-polarized tumor cells. Pan-FGFR inhibitor NVP-BGJ398 (Infigratinib) reversed the SHHi-induced EMT marker expression and nuclear FGFR1 accumulation without compromising the enhanced permeability effect.

Conclusion: This dual-hit strategy of SMO and FGFR inhibition provides a clinically-translatable approach to compromise the profound impermeability of PDAC tumors. Furthermore, clinical deployment of DW-MR imaging could fulfill the essential clinical-translational requirement for patient stratification.

Introduction

Five-year survival is a dismal 9% for the 80% of pancreatic cancer (PDAC) patients having metastatic, inoperable, or borderline-resectable tumors at diagnosis(1). Neoadjuvant therapy may enable surgical resection and improve survival(2), but tumor hypovascularity and desmoplasia remain formidable barriers to drug delivery and contribute to PDAC treatment resistance(3). Activation of hedgehog (HH) ligand secretion in tumor cells stimulates paracrine activation of HH pathway signaling in the stromal compartment, driving fibrosis and desmoplasia(4,5). Targeting HH signaling using Smoothened (SMO) inhibitors (SHHi) degrades the fibrotic tissue scaffold and increases vascular perfusion and permeability, priming PDAC tumors for enhanced delivery and efficacy of both small-molecule- and macromolecular therapeutics(3,6,7). However, clinical studies have reported a lack of clinical survival benefit for SHHi combined with gemcitabine or FOLFIRINOX(8,9). In parallel, preclinical studies established that chronic ablation of HH signaling by pharmacological inhibtion, by genetic deletion of sonic HH ligand (Shh) in tumor cells, or by genetic depletion of stromal HH ligand targets, such as carcinoma-associated fibroblasts (CAF), interrupts tumor-stroma crosstalk in such a way as to release stromal restraint over tumor cells, which promotes tumor de-differentiation and initiates epithelial-to-mesenchymal transition (EMT) (10-12). Other HH ligands such as Indian HH (Ihh) also contribute to promoting HH signaling in CAF (13). Implementing intermittent rather than chronic SHHi treatment could reduce EMT drive and avoid rapid onset of pharmacodynamic tolerance that abrogates the tumor priming effect(6,7,14). Ultimately, strategies to mitigate EMT-promoting signaling resulting from SMO inhibition, and approaches for identifying those patients whose tumors respond with increases in perfusion/permeability, could advance the clinical success of PDAC tumor priming strategies.

Because treatment strategies that induce the enhanced permeability and retention (EPR) phenomenon favor tumor delivery and retention of higher molecular-mass agents(15,16), we developed a sequential strategy combining short-term SHHi pretreatment with therapeutic antibodies or cytotoxic nanoparticles that increases their delivery and efficacy in histopathologically-diverse PDAC patient-derived xenografts (PDX) that recapitulate the desmoplasia and low vascularity of clinical tumors(6,7). To facilitate investigation of inter-individual variabilities in tumor perfusion/permeability responses to SHHi, we developed a noninvasive alternative to dynamic contrast-enhanced magnetic resonance imaging (DCE-MRI), which has minimal sensitivity to detect SHHi-mediated effects on PDAC tumors. In parallel, we assessed the near-term effects of SHHi on blood/tumor barrier permeability/perfusion and extracellular matrix (ECM) structure. We also investigated the mechanisms by which HH inhibition promotes EMT and approaches to reverse it, based upon on preliminary data suggesting that HH ignaling inhibition activates fibroblast growth factor receptor (FGFR) signaling, and reports that small-molecule FGFR inhibitors (FGFRi) promote mesenchymal-to-epithelial transition in metastatic breast, colon, and prostate cancers(17-20).

Materials and Methods

Animals and Reagents

SCID mice (C.B-lgh-1^{b}/lcrTac-Prkdc^{scid}) were obtained from Roswell Park Comprehensive Cancer Center (Buffalo, NY). The SHHi NVP-LDE225 was from ChemieTek (Indianapolis, IN). NVP-BGJ398 (pan FGFRi) was from Novartis. *Supplementary Table S1* describes the antibodies used for immunostaining and analysis.

Cell lines and Cell Culture

The human pancreatic cancer cell lines obtained from ATCC (American Type Culture Collection, Manassas, VA) were PANC-1 (RRID:CVCL_0480; ATCC CRL-1469) and MIAPaCa-2 (RRID:CVCL_0428; ATCC CRL-1420). Cells were cultured in DMEM (Cellgro, Manassas, VA) supplemented with 10% (v/v) fetal bovine serum (Cellgro) and subcultured upon reaching confluence. Cell line authentication was performed by STR analysis at the Roswell Park Gene Modulation Core, and mycoplasma testing was performed by the Roswell Park Genomics Core.

Tumor models and experimental design

Animal studies were approved in advance by the Institutional Animal Care and Use Committees (IACUC) of the University at Buffalo, State University of New York, and the Roswell Park Comprehensive Cancer Center. PDAC PDX tumors were propagated as described(21). Tumor fragments from donor mice were implanted *sc*, where they retain key patient-like histological and drug delivery barrier properties ((6,7); *Supplementary Methods, Supplementary Fig. S1*). Invasive PDAC PDX models #18269 (pathology grade G2, moderately-differentiated), #18254 (G3; poorly-differentiated), and #14312 (G2-G3 poorly-differentiated) were selected based on their significant differences in stromal content, histology, and growth characteristics. When tumors reached 200-250 mm^3, mice were randomized into groups having equivalent mean tumor volumes and treatment protocols described were initiated. Power analysis of prior experiments informed group sizes. At intervals during/after treatment, vascular permeability, ECM characteristics, and tumor responses were assessed. Tumor diffusivity was measured by diffusion-weighted (DW) magnetic resonance (MR) imaging, and high phase-transition sterically-stabilized liposomes (SSL) of 80-100 nm, labeled with the nonexchangeable

fluorescent probe DiI(6) (SSL-DiI), were injected *iv* as vascular permeability probes immediately after acquiring MR scans. At the time of peak SSL deposition (24h post-dose), fluorescent *Lycopersicon esculentum* lectin (Millipore-Sigma, St. Louis, MO; 8 mg/kg) was injected *iv* to probe vascular function. After 10 min, tumors were rapidly harvested, frozen in nitrogen, and serially-sectioned for analysis. Because of the MR imaging times required, 3-4 mice/group/time-point were employed, and studies were replicated twice. *Supplementary Methods* provides additional experimental details on tissue imaging and permeability assessment.

MRI and image processing

MRI scans were acquired using a small-bore 4.7 Tesla Bru¨ er (Billerica, MA) preclinical imaging system using a 35mm I.D. quadrature radiofrequency coil (M2m Imaging, Cleveland OH) and ParaVision3.0.2 acquisition software (RRID:SCR_001964; Bru¨ er). T1-weighted images were acquired at intervals before and after *iv* injection of Gadolinium-DTPA (100μmol/kg), and T1 relaxation rates were determined using an inversion-recovery TrueFISP acquisition protocol (*Supplementary Methods*). Non-directional DW-MRI measurements were acquired using axial, spin-echo diffusion scans. A chemical shift-selective, fat-suppression preparatory pulse was included to minimize adipose tissue signal (*Supplementary Methods*). For analysis, tumor regions of interest (ROI) were created for each image dataset using Analyze10.0 (RRID:SCR_005988Analyze Direct, Overland Park, KS), and diffusion maps for each ROI were created using in-house MATLAB routines (RRID:SCR_001622; MathWorks, Natick, MA) by fitting the data on a voxel-by-voxel basis to a mono-exponential equation that derived the Apparent Diffusion Coefficient (ADC) based on the signal intensity and magnetic gradient strength. Mucinous vacuoles within the tumor showed considerably higher ADC values than cellular regions, and were eliminated from ADC maps using a MATLAB thresholding algorithm,

with visual confirmation of results by histogram inspection. *Supplementary Methods* provides additional details on imaging and analysis.

Tumor imaging and western blotting

Supplementary Methods details immunostaining and imaging of frozen tumor sections, and acquisition of high-magnification z-stacked confocal images for colocalization studies and inter-leaved fluorescence- and second-harmonic images of tumor sections. Confirmation and quantification of specific target proteins was by western blotting from Tris-Bis gradient gels (*Supplementary Methods, Supplementary Table S1*).

Image processing and feature correlation

Fluorescent probe deposition in tissue images was quantified from panoramic images measuring ~1.5 mm x 1.5 mm (N=2-3 sections/tumor, 3-8 images/tumor section, depending on tumor size, or alternatively ~80% of the whole tumor section) using *Fiji* software (RRID:SCR_002285; (22)) (*Supplementary Data*). Correlation and colocalization of FGFR1 (labeled with AlexaFluor 594 antibody) with $DAPI^+$ nuclei was performed on background-subtracted confocal z-stack images (z=5 x 2 μm slices from 5-10 ~0.7 mm x 0.7 mm panoramas/section) using the *Fiji coloc2* plugin. Costes' regression (PSF=3; Costes' randomizations=50) was employed to test correlations(23), and we report Mander's split coefficient with Costes' threshold (tM_n), relating intensity of significantly colocalized voxels.

RNA sequencing and ChIP-seq analysis

Total RNA was extracted, reverse-transcribed, and subjected to next generation sequencing. *Supplementary Data* provides detailed procedures, software, and the workflow to extract species-specific mouse (stromal) and human (tumor cell) transcripts(24). Data identifying DNA

sequences binding the nuclear-localizing fragment of FGFR1 (nuFGFR1) were mined from a published report on human neuronal progenitor cells(25). *Supplementary Data* describes gene set enrichment analysis.

Statistical testing

Statistical testing employed Prism7.0 (RRID:SCR_000306; Graphpad, LaJolla, CA) for non-transcriptomic data, and included unpaired, one-tailed Student t-tests, with Welch's correction where necessary to assume unequal standard deviation between groups.

Data availability

RNA-Seq data were generated by the Functional Genomics Group of Queens University Belfast, UK, led by Dr. S.S. McDaid, and have been deposited in the NCBI Gene Expression Omnibus GEO and Sequence read archive (RRID:SCR_005012; https://www.ncbi.nlm.nih.gov/geo/query/acc.cgi?acc=GSE159334). Derived data supporting the findings of this study are available from the corresponding author upon request.

Results

Short-term SHHi treatment rapidly alters ECM structure and tumor permeability

PDAC PDX models were selected to investigate SHHi treatment effects upon tumor architecture and biology owing to their superior recapitulation of both patient inter-individual variability and the complex autocrine/paracrine signaling networks among the heterogenous cell populations within tumors involved in HH signaling. In subcutaneously-implanted PDX tumors that retain the cellular differentiation, low MVD, and permeability/perfusion of clinical PDAC tumors, we observed previously(6,7) that short-duration treatment with the SMO inhibitor NVP-

LDE225 increased tumor vascular perfusion and permeability, doubling the deposition of sterically-stabilized, Doxil®-like liposomes containing doxorubicin (SSL-DXR) and tripling delay of tumor progression. SHHi priming also doubled tumor deposition of anti-EGFR cetuximab, which mediated sustained tumor suppression.

To investigate inter-individual variability in SHHi responses among histopathologically diverse patient isolates, we selected three invasive PDAC models: PDX #18269 (high MVD/high-stroma), #18254 (low MVD/high-stroma), and #14312 (medium MVD/low-stroma) (Supplementary Fig. S1A-C). Second harmonic generation (SHG) microscopy of unstained tumor sections demonstrated that the three PDXs differed in fibrillar collagen abundance based on total SHG signal; high stroma tumors #18269 and #18254 contained 11% and 8% fibrillar collagen, and low stroma #14312 contained 5% (Supplementary Fig. S1D-H)). The doubling time of the high-stroma tumor models was nearly 2-fold longer that of low-stroma tumor #14312, in which expression of EMT marker N-cadherin was nearly double (*Supplementary Fig. S1I-J, Supplementary Table S2*; (21)).

Short-term treatment with SHHi NVP-LDE225 (40 mg/kg/day *po* for 7-10) days reduced both mouse (stromal cell) and human (tumor cell)-derived Gli1 expression in both high-stroma tumor models, #18269 and #18254 (*Supplementary Fig. S2A*), and represented the minimum dose and duration necessary to enhance tumor permeability. Fluorescent 80nm SSL-DiI, which are surrogates for nanoparticulate drug carriers such as Doxil® and Onivyde® (liposomal irinotecan;(26)) in terms of size and drug cargo capacity, were administered *iv* at intervals during SHHi priming to probe vascular permeability, and tumors were harvested 24h later, at the peak of SSL deposition. SHG was used to investigate SHHi treatment responses at a histological level, and confocal microscopy allowed colocalization of SSL-DiI deposition with SHG signal

(*Supplementary Fig. S2B-E*). Forward-transmission SHG (F-SHG) was used to image thick collagen fibers, and backward-transmission SHG (B-SHG) captured the signal emanated by off-phase, thin collagen fibers that are a hallmark of regenerative tissue undergoing rapid collagen turnover(27). All three PDX tumors displayed thick collagen fibers that generated a stronger F-SHG signal than B-SHG, and had F-SHG:B-SHG ratios of approximately 3 (*Supplementary Fig. S2F-H*).

PDX tumors #18269 and #14312 responded to daily SHHi treatment with both increased nanoparticle deposition and a significant (2-fold) decline in F-SHG:B-SHG ratio after 4-8 days of treatment compared to controls (*Supplementary Fig. S2F-H*), indicating that SHHi treatment depleted the ECM while increasing the abundance of thin collagen fibrils, which is associated with stromal remodeling and pro-invasive characteristics(27). SHHi treatment did not increase SSL-DiI deposition in PDX #18254 nor change the F-SHG:B-SHG ratio.

To determine whether ECM depletion correlated with enhanced tumor permeability, the magnitude and intratumor distribution of SSL-DiI deposition was quantified during SHHi dosing (*Supplementary Fig. S3*). SHHi pretreatment increased significantly the area of nanoparticle deposition in SHHi-responsive PDXs #18269 (*Supplementary Fig. S3A-C;* $p<0.05$) and #14312 (*Supplementary Fig. S3E,F;* $p<0.05$) compared to vehicle controls, but decreased the magnitude and area of SSL-DiI deposition in SHHi-refractory PDX #18254 (*Supplementary Fig. S3H,I*; $p<0.05$).

Deposition of *iv*-injected SSL-DiI was lower in regions of thick collagen fibers (higher F-SHG signal), and higher in regions of thinner collagen fibrils (higher B-SHG signal; *Supplementary Fig. S2F-H*). SHHi-treated tumors had fewer fibrous regions, which permitted more extensive stromal nanoparticle penetration (*Supplementary Fig. S2B-E*). Our previous

quantification of total ($CD31^+$) *vs.* functional (L. esculentum$^+$ lectin) tumor vasculature showed that the SHHi dose and treatment duration employed here increases functional- but not total MVD (6,7). Depletion of fibrillar collagens would contribute significantly to SHHi-augmented tumor perfusion by alleviating mechanical strain within the ECM, reducing intra-tissue pressure, and restoring vascular patency, resulting in increased deposition, intra-tumor distribution, and therapeutic efficacy of chemotherapy, as we observed previously with nanoparticles and antibodies (6,7).

Tumor ADC and permeability increase in parallel during SHHi-treatment

DCE-MRI demonstrated that unperturbed *sc* PDAC PDX tumors show minimal Gd-DTPA contrast enhancement, in stark contrast with well-perfused, cell-line-based tumor models (Fig. 1A). Furthermore, conditions under which SHHi treatment significantly increased tumor nanoparticle deposition resulted in negligible contrast enhancement by the macromolecular vascular perfusion probe Gd-albumin (Fig. 1B). Apparent diffusion coefficient (ADC), which quantifies interstitial water mobility based upon diffusion-weighted (DW)-MRI, is sensitive to the organization and tortuosity of extravascular tissue (28,29) and correlates inversely with fibrosis in PDAC (28).

To test the hypothesis that SHHi-mediated fibrosis reduction increases tumor interstitial water mobility, we investigated whether ADC is responsive to temporal changes in ECM and tumor perfusion/permeability during SHHi priming. In SHHi-responsive tumor #18269, 3d and 7d of SHHi dosing significantly increased both absolute ADC (Fig. 1C,D) and ADC relative to its pretreatment value (rADC; Fig. 1E, *Supplementary Fig. S3D*), whereas in tumor #14312, absolute ADC did not change (*Supplementary Fig. S3G*), but rADC increased within 3d of

treatment (Fig. 1F, $p<0.01$). In non-responsive tumor #18254, SHHi treatment changed neither absolute nor rADC significantly (Fig. 1G, *Supplementary Fig. S3G,J*).

To compare tumor ADC changes with changes in permeability and nanoparticle delivery, SHHi-treated animals were injected with fluorescent SSL-DiI nanoparticles immediately after acquiring DW-MRI scans, and deposition was quantified 24h later. For all PDXs, the ADC of each animal's tumor correlated linearly with the magnitude of nanoparticle deposition (Fig. 1H-J, *Supplementary Fig. S3C,F,I*), establishing a link between ADC and tumor microenvironmental factors controlling SSL delivery.

We also investigated whether therapeutic responses reflect the observed alterations in tumor diffusivity and SSL-DiI deposition. Three cycles of sequential SHHi priming followed by SSL-DXR were administered to priming-responsive PDX #18269 and priming-refractory #18254 (Fig. 1K-N). Neither single-agent SHHi nor SSL-DXR affected volume progression in #18269, but as observed previously(6), and as the increased ADC would predict, sequential SHHi/SSL-DXR reduced tumor progression significantly relative to all other treatments ($p<0.05$; Fig. 1K,L). In contrast, single-agent SHHi suppressed #18254 tumor progression, but single-agent SSL-DXR had no significant effect (Fig. 1M,N), as the lack of SSL-DiI deposition would predict. Sequential SHHi/SSL-DXR was no more effective than SHHi alone, as the unchanged rADC and lack of enhanced nanoparticle deposition would predict. In PDAC, HH signaling participates in complex paracrine crosstalk among tumor and stromal cell populations, and drives increased tumor cell proliferative capacity and resistance to apoptosis (30). PDX #18254 is the highest-EGFR-expressing, most epithelioid tumor evaluated, with a very low MVD. Its differential responses to SHHi and SSL-DXR likely arise from individual tumor differences in reliance on

HH signaling for proliferation *vs.* stromal integrity, and the lack of appreciable tumor priming and SSL-DXR delivery to PDX #18254 under any condition.

SHHi treatment alters ECM structure and cellular density, and both affect ADC (29). Therefore, tumors sections were co-stained to quantify collagen I and human mitochondrial proteins (huMITO), which identify tumor cells (Fig. 2). In SHHi-responsive models #18269 and #14312, SHHi treatment decreased collagen I significantly, and the ADC value for each individual tumor correlated inversely with its tumor collagen I mass (Fig. 2A-F; $p<0.05$). Priming non-responder tumor #18254 was negative for the fibrillar collagen structural changes that were observed in SHHi priming responders. Notably, the overall density of tumor- and stromal cell nuclei remained unchanged (Fig. 2G), suggesting that SHHi-mediated increases in ADC and nanoparticle penetration result from ECM remodeling rather than changes in tumor cell density.

Together, these data support ADC as a surrogate marker for SHHi-mediated enhancement of both tumor permeability and cytotoxic nanoparticle delivery. Given that the SHHi treatment conditions employed here mediate therapeutically-meaningful changes in tumor permeability that were undetectable by DCE-MRI, but detectable by DW-MRI, and that ADC both detects inter-patient variability in SHHi-mediated priming and predicts therapeutic response to priming(Fig. 1; (6,7)), DW-MRI has potential as a clinically-deployable tool for patient stratification and clinical optimization of tumor priming regimens.

EMT and local inflammatory responses accompany short-term SHHi treatment

SHHi treatment mediated drastic changes in tumor architecture. Untreated #18269 tumors showed abundant collagen I-rich stroma surrounding glandular structures lined by well-

differentiated adenocarcinoma (huMITO$^+$) cells (Fig. 2A). However, SHHi-treated tumors showed reorganized glandular structures of reduced area that were replete with papillary projections and situated within narrow collagen I domains. Prominent tumor cell clusters were also observed in stromal regions. Whereas PDX #14312 controls showed moderately-differentiated tumor cells separated by narrow bands of collagen I, SHHi treatment resulted in enlarged clusters of poorly-differentiated tumor cells associated with regions of markedly-reduced collagen I (Fig. 2B). In both models, SHHi treatment increased the area occupied by tumor cells and decreased stromal area, but the total (tumor+stromal) cellular density remained comparable among treatment groups during SHHi treatment ($p<0.05$; Fig. 2H-K).

Given the histologically-observed reorganization of SHHi-treated PDXs, and that HH signaling ablation induced EMT, we investigated SHHi effects on the expression of EMT markers N-cadherin and vimentin using a knockout-validated anti-human vimentin antibody that does not cross-react with murine vimentin (Fig. 3). In PDX #18269, vimentin$^+$ tumor cell invasion of stromal regions increased 3-fold over 8d of SHHi treatment (Fig. 3A,B,E; $p<0.001$), as did the fraction of N-cadherin$^+$/huMITO$^+$ cells (*Supplementary Fig. S4A-H;* $p<0.0001$). PD-L1$^+$ cells also increased within vimentin$^+$ tumor cell clusters in SHHi-treated tumors (*Supplementary Fig. S4I-K*). Proliferating (Ki67$^+$) tumor cells resided mostly in proximity to glandular structures rather than in the stroma, and doubled after 8d of SHHi treatment (Fig. 3C,D,F; $p<0.0001$). The low-stroma #14312 tumor, which expressed nearly 2-fold higher baseline N-cadherin than did the #18269 model, increased further with SHHi treatment (*Supplementary Fig. S4F*; $p<0.05$). Increased expression of EMT markers by antagonists of HH signaling is consistent with prior reports that genetic ablation of Shh ligand, pharmacological antagonism of HH signaling, and stromal cell (CAF) ablation all induce cellular de-

differentiation and EMT *via* disruption of paracrine tumor-stroma crosstalk and stromal cell depletion/deactivation(10-12). Notably, Ihh ligand production by tumor cells also stimulates HH signaling in stromal fibroblasts (13)

RNA-Seq analysis of SHHi-responder #18269 was performed to identify key protein expression changes that drive the tissue-level responses observed during SHHi-mediated priming (*Supplementary Table S3*). Because PDX tumors are chimeras, in which tumor cells are human and stromal cells are murine, species deconvolution of RNA-Seq data permitted identification of differential responses of the tumor and stromal compartments to HH signaling inhibition. Gene set enrichment analysis (GSEA) of differentially-expressed genes revealed that SHHi treatment significantly enriched hallmark tumor-derived (human) genes associated with EMT, pro-inflammation (IL2-STAT5 signaling, IFN-γ receptor heterodimers), pluripotency (OCT4, NANOG; Fig. 3G-I*; Supplementary Table S4*; q-value<0.05), and cell cycle arrest, based on E2F DNA replication targets and G2M checkpoints.

Fig. 3J-L presents a heatmap of differentially-expressed genes belonging to the hallmark clusters EMT, IL2/STAT5, and G2M checkpoint. Gene ontology (GO) analysis (*Supplementary Table S5*) identified epithelial morphogenesis and EMT as pivotal clusters enriched by SHHi treatment associated with significant changes in genes associated with cell polarity and mesenchymal phenotype (*Supplementary Fig. S5*). Control *vs.* SHHi-treated samples segregated based on the expression of EMT and inflammation genes, but not G2M checkpoint genes, suggesting that SHHi treatment exerted greater influence on EMT and inflammation.

FGFR1 signaling increases in SHHi-treated tumors

Signal transduction during HH signaling inhibition was analyzed in PDX #18269 as a representative SHHi-responsive tumor. Among common pro-EMT signals, TGFβ pathway

protein expression was downregulated (TGFβ-inducible protein TGFBI; *Supplementary Table S4*; p<2e-5), with no evidence of Wnt signal activation, suggesting an alternate mechanism of EMT induction in SHHi-treated tumors. Transcription factor/ upstream master regulator enrichment analysis (*Supplementary Table S6, Supplementary Fig. S6A,B*), and kinase enrichment/upstream regulator analysis (*Supplementary Fig. S7A,B*) implicated key receptor kinases as drivers of SHHi-mediated phenotypic alterations. Among the predicted kinase activations, only mRNA of MAPK3/Erk1, a known EMT-inducer (31,32), was elevated in SHHi-treated tumors (Fig. 4A-C; p<0.01). As expected for KRAS-driven tumors, almost all tumor cells stained positively for nuclear p-Erk1/2, which was slightly higher in the SHHi-treated tumors. Upstream of Erk1, genes associated with FGF family signaling showed the greatest deregulation, and FGFR1 protein and mRNA were elevated significantly (Fig. 4D; p<0.01). SHHi treatment also changed the expression of FGFR1-ligands significantly, downregulating tumor FGF2 and upregulating stromal FGF1, suggesting that stromal FGF may drive FGFR1 signaling in tumor cells (Fig. 4E,F; p<0.05) and EMT (33).

FGFR1 promotes tumor cell migration by multiple mechanisms in PDAC and other cancers. Pharmacological inhibition of FGFR1 inhibits EMT (17,18,34-36), and clinical data demonstrate that PDAC tumor FGFR1 expression correlates positively with EMT markers vimentin, SNAI1, and ZEB1 (*Supplementary Fig. S8A-C*). After 8d of SHHi treatment, FGFR1 expression was elevated significantly in PDX #18269 tumors (Fig. 4G,H). Confocal 3D-imaging of vehicle-treated controls revealed that FGFR1 expression was largely confined to the cytoplasm of tumor cells, but SHHi treatment resulted in a striking redistribution of FGFR1 to tumor cell nuclei (Fig. 4I,J). The speckled distribution pattern of nuclear FGFR1 (nuFGFR1) staining resembles transcription factor distribution at RNA processing sites (37). Treatment with SHHi doubled

nuFGFR1 ($p<0.001$) in tumor cells, but not in stromal cells (Fig. 4K), suggesting differential responses of tumor *vs.* stromal compartments to SMO inhibition.

Nuclear FGFR1 signaling has been implicated in driving invasiveness and promoting therapeutic resistance *via* transcription of EMT-associated genes in PDAC and breast cancers (34-36,38). To explore whether nuFGFR1 might bind to promoter regions of pro-EMT genes, we mined a publicly-available ChIP-Seq dataset in which an anti-FGFR1 antibody was used to immunoprecipitate protein-DNA complexes from human neuronal progenitor cells (25). We hypothesized that the genomic structure and transcriptional machinery of pluripotent human embryonic stem cells would share some degree of commonality with other human cells, including human PDAC cells. Data mining suggested the Erk-1 promoter region as a transcriptional target of FGFR1 (Fig. 4L), implicating nuFGFR1 signaling in driving EMT *via* increased Erk-1 transcription. GSEA of nuFGFR1-bound-genes in the neuronal progenitor cell dataset showed an enrichment of hallmark gene clusters similar to functional clusters that were enriched in SHHi-treated tumors, including EMT, G2M checkpoint, UV response, and E2F targets (*Supplementary Fig. S9A*). Seventeen genes were shared between our RNA-Seq dataset of SHHi-upregulated genes and the transcriptional targets of FGFR1 identified in the human neuronal progenitor cell ChIP-Seq dataset, including MAPK3/Erk-1 (*Supplementary Fig. S9B,C*). These findings merit detailed investigation in additional PDAC PDX models. Interestingly, confocal image sections passing through the plane of nuclei showed that mesenchymal (vimentin$^+$) tumor cells were nuFGFR1$^+$ in both vehicle- and SHHi-treated groups (Fig. 3A,B), whereas proliferating (Ki67$^+$) cells were negative for nuFGFR1 (Fig. 3C,D). The conspicuous pattern of FGFR1 subcellular localization in phenotypically distinct cells

(vimentin$^+$/nuFGFR1$^+$ *vs.* Ki67$^+$/nuFGFR1$^-$) suggests a possible relationship between FGFR1 expression and phenotype that merits future exploration.

Pan-FGFR inhibitor reverses EMT markers

To test the hypothesis that FGFR1 signaling plays a significant role in driving the phenotypic changes observed in PDAC tumors following SHHi treatment, the pan-FGFRi NVP-BGJ398 (infigratinib), which has >100-800-fold greater potency for FGFR1-3 over other kinases (39,40), was administered daily for 3d to animals bearing SHHi-responsive PDXs #18269 and #14312 after 7d pretreatment with SHHi or vehicle (Fig. 5, S10). As in Fig. 2, SHHi-treated tumors showed drastically reorganized glandular structures within 8d of treatment, with prominent tumor cell clusters increased significantly in stroma-dense regions (Fig. 5A, *Supplementary Fig. S10A-C,F-H,K*; $p<0.01$). In vehicle controls, single-agent FGFRi decreased the area occupied by tumor cells in PDX #18269 slightly but significantly (Fig. 5A,B; *Supplementary Fig. S10E,J,K;* $p<0.05$) but did not alter the number of vimentin$^+$ or Ki67$^+$ cells (Fig. 5C-E). In PDX #14312, which has higher baseline expression of mesenchymal features such as N-cadherin, single-agent FGFRi reduced both N-cadherin expression and the area occupied by tumor cells (*Supplementary Fig. S11A-F;* $p<0.05$), suggesting greater activity of single-agent FGFRi in high-EMT models (41). Notably, FGFR1 expression levels also correlate inversely with PDAC tumor sensitivity to single-agent FGFRi (41). After 7d of SHHi treatment, 3d of FGFRi treatment altered #18269 tumor architecture markedly, largely restoring an epithelioid tumor cell phenotype, reverting the densely-folded glandular structures to a histological organization resembling controls, and reducing the area occupied by tumor cells, including tumor cell colonies embedded in stroma (Fig. 5A,B, *Supplementary Fig. S10A-I,K*; $p<0.001$). Similar results were observed in #14312 tumors (*Supplementary Fig. S11A-E*). In both

models, sequential SHHi+FGFRi treatment restored collagen I organization to a control-like morphology (Fig. 5A,B; $p<0.001$; *Supplementary Fig. S11A-D*).

Sequential SHHi+FGFRi treatment reduced the EMT and proliferation markers that single-agent SHHi treatment upregulated. In PDX #18269, this dual-hit treatment reduced vimentin$^+$ tumor cells 3-fold ($p<0.001$), and Ki67$^+$ tumor cells 1.3-fold ($p<0.05$) compared to single-agent SHHi, and returned vimentin and Ki67 to control levels (Fig. 5C-E). Similar results were obtained in tumor #14312 with N-cadherin as an EMT marker (*Supplementary Fig. S11F*; $p<0.05$).

In the MAPK pathway, both Erk1/2 and phospho-Erk1/2 were upregulated by SHHi treatment, and sequential SHHi+FGFRi reduced both, with a significantly greater inhibitory effect on total Erk1/2 than on p-Erk1/2 (Fig. 5F,G), suggesting that reduced Erk1/2 expression reduced EMT drive. Single-agent SHHi did not alter Mek1/2 and p-Mek1/2 levels from control levels, but sequential SHHi+FGFRi increased p-Mek1/2 expression (Fig. 5F,G). The discordant FGFRi effects on Erk/p-Erk *vs.* p-Mek (inhibitory *vs.* enhancing) suggest a deviation from canonical MAPK signaling.

Sequential SHHi+FGFRi treatment also reversed the nuFGFR1 elevation prevalent in tumor cells after single-agent SHHi treatment, restoring predominantly-cytoplasmic FGFR1, although overall FGFR1 expression remained elevated (Fig. 5E), suggesting that the FGFRi did not inhibit FGFR1 expression. Given the FGFRi-mediated reversal of changes in EMT markers and tumor morphology in parallel with the subcellular redistribution of FGFR1, nuFGFR1 likely plays a role in regulating EMT in PDAC cells. Similar findings were reported in breast cancer, where nuFGFR1 drove both EMT and estrogen resistance by partnering with transcriptional factors and binding directly to genomic transcription sites (34,35). In treatment-naïve tumors, FGFRi

mediated a slight enhancement of MAPK components, but reduced nuFGFR1 significantly compared to controls (Fig. 5E,G), suggesting the inhibitory effect of FGFRi on EMT markers may be associated with the altered subcellular localization of FGFR rather than changes in canonical MAPK signaling.

Dual-hit HH/FGFR inhibition sustains elevated tumor perfusion and permeability

Given that FGFRi treatment reversed numerous SHHi-mediated phenotypic changes that occurred in parallel with tumor priming, we investigated whether the SHHi+FGFRi sequence abrogated the beneficial effect of SHHi upon tumor perfusion/permeability. Three days of single-agent FGFRi treatment did not significantly alter tumor vascular permeability, the number of functional vessels, nor deposition of 80 nm probe SSL-DiI, although focal regions of extravasation increased slightly (Fig. 6A,B). In contrast, 7d of SHHi treatment nearly doubled the number and size of functional vessels, tripled the area perfused by functional vessels, and increased nanoparticle probe deposition 1.5-fold compared to controls (Fig. 6C-F; $p<0.05$). Notably, after 11d of single-agent SHHi treatment, functional vessel size, area perfused by functional vessels, nanoparticle deposition, and tumor ADC were all reduced significantly (Fig. 6G-H; $p<0.05$), consistent with onset of pharmacodynamic tolerance to the SHHi priming effect and restoration of the drug delivery barrier. The dual-hit sequence of 7d SHHi treatment followed by 3d of FGFRi forestalled tolerance and maintained tumor perfusion and permeability, such that nanoparticle deposition, functional vessel size, and tumor area perfused were undiminished compared to peak levels observed after d8 of single-agent SHHi. Therefore, even though the SHHi+FGFRi dual-hit sequence restored collagen I to control-like morphology (Fig. 5a), the drug delivery barrier had not been restored. In fact, sequential SHHi+FGFRi increased functional vessel density, and tumor ADC increased by 25-40% compared to single-agent SHHi

($p<0.05$), resulting in the highest observed values of rADC (Fig. 6H). As observed with single-agent SHHi, ADC values for individual mice correlated linearly with their observed SSL-DiI deposition (Fig. 6I), regardless of treatment group. Collectively, the data demonstrate that FGFRi post-treatment of SHHi-primed tumors reversed the deleterious effects of HH signaling ablation, delayed the onset of pharmacodynamic tolerance, and maintained the patency of functional vessels while sustaining, if not enhancing, the beneficial effects of SHHi treatment on nanoparticle delivery.

Discussion

The fibrotic tissue scaffold that develops in PDAC unquestionably contributes to inadequate drug delivery and failure of chemotherapy(42,43). Conceptually, tumor priming approaches for compromising tumor drug delivery barriers represent a promising strategy, but clinical development has been challenging(3,6,44). Systemic PEG-hyaluronidase showed preclinical potential, lowering intra-tumor pressures and increasing permeability(45), but adverse thromboembolic events led to its clinical withdrawal(46). Angiotensin receptor inhibitor losartan reduces stromal collagen and pro-fibrotic TGF-β signaling; positive clinical results were obtained for conversion of borderline-resectable patients to resectable, but no benefit was observed with metastatic PDAC(47,48). Additional strategies to improve tumor priming and translating them clinically are essential.

Pharmacological inhibition of paracrine HH signaling by SMO inhibitors, which interdict HH signaling downstream of HH receptors, primes PDAC tumors, increasing perfusion and EPR-mediated deposition. Although deposition of conventional small-molecule drugs increases with SHHi treatment(3), they can clear rapidly from tumors owing to their high diffusion coefficients. Macromolecular agents such as antibodies and nanoparticulate drug carriers have

much lower diffusion coefficients and clear more slowly from the fibrotic ECM, theoretically rendering them superior in combination with treatments that increase EPR-mediated delivery(15). Some nanoparticle carrier formulations additionally have very large cargo capacities and can establish persistent intratumor drug depots for sustained drug delivery. These effects would be amplified by tumor priming strategies that increase accessibility of the tumor interstitium for delivery *via* EPR. Short-term SHHi priming approximately doubles nanoparticle deposition in poorly-vascularized PDAC PDX tumors, leading to a striking 3-fold increase in median survival with drug-loaded nanoparticles(6). Newer formulations such as Onivyde®(49) add to the diversity of clinically-available nanoparticle formulations. SHHi priming also increases PDAC tumor deposition and efficacy of antibodies(7). However, clinical evidence for SHHi effects on tumor perfusion/permeability is elusive(8,9), which results here suggest may derive from insensitivity of imaging methods to detect the types of biophysical changes in tumors that result from HH signaling inhibition. In addition, preclinical models show that chronic inhibition of HH signaling increases tumor invasiveness(10,11).

To minimize adverse SHHi responses, maximize chemotherapeutic exposure, and avoid pharmacodynamic tolerance, we developed a strategy of minimizing the intensity and duration of SHHi exposure, imposing a drug-free holiday between treatment cycles, and exploiting the advantages of macromolecular drugs and carriers(6,7). Through detailed examination of SHHi effects on PDAC tumors, we identified rewired cancer signaling that contributes to pro-invasive effects of HH-treatment, and demonstrate that selective, clinically-approved FGFR kinase inhibitors reverse deleterious tumor responses to SHHi while sustaining the priming responses that improve nanoparticle delivery. In addition, we identified a noninvasive imaging approach

that could enable stratification of priming-responsive patient tumors. These developments together suggest a new path toward successful clinical deployment of tumor priming strategies.

The inter-individual variability we demonstrate in PDAC PDX responses to SHHi treatment suggests that individualization of therapy is essential. We found that DCE-MRI is unable to detect subtle but therapeutically-important alterations in tumor permeability/perfusion accompanying priming, but that DW-MRI reports priming-mediated biophysical changes occurring in the ECM that increase intra-tumor water mobility and correlate with increased tumor accumulation of macromolecular therapeutics. This increased intra-tumor water mobility is reflected in ADC, providing an MR-imageable, non-invasive marker for SHHi-mediated priming. Relative tumor ADC and nanoparticle deposition increased in parallel in SHHi-responsive PDX tumors, whereas non-responder tumors showed no change in relative ADC and little nanoparticle deposition. We also observed that enhancement of perfusion/permeability coincided with both reduction of stromal fibrosis, which manifests as increased ADC and drastic increases in tumor vessel patency (Fig. 6;(7)). For these reasons, DW-MRI measurement of ADC surpasses sensitivity limitations of DCE-MRI for discerning key priming-mediated ECM alterations that occur at a sub-millimeter scale, and is a clinically-deployable imaging protocol by which to stratify patients, and aid development and optimization of tumor priming therapies.

In parallel to enhanced tumor diffusivity, SHHi treatment also evoked a proinflammatory response in which the tumor ECM underwent a transition from thicker collagen fibers to more isotropically-organized thin collagen fibers, which has been associated with increased cancer cell motility(27,50). Remodeling of the collagen-rich ECM led to increased EMT markers and an abundance of mesenchymal tumor cells within the ECM. Therefore, limiting the duration of SHHi exposure may reduce deleterious effects. In murine PDAC models, chronic exposure to

SHHi, or genetic deletion of Shh ligand in tumor cells, reduced fibrosis markers (*eg.* collagen I and αSMA^+ fibroblasts), thereby driving EMT and increasing invasiveness and malignancy(10,11). Activation of other HH ligands, such as Ihh, also contributes to phenotypic signaling derangements (13). Conversely, pharmacological HH signaling *agonism* increased desmoplasia, fibrosis markers, and epithelial differentiation, resulting in decreased malignancy. The demonstration that genetic deletion of αSMA^+ PDAC cancer-associated fibroblasts promotes EMT, reduces fibrosis markers, and accelerates disease confirms the paracrine nature of the signaling network through which HH agonism restrains PDAC, and that HH antagonism drives EMT(12). Here we show that the paracrine signaling network through which HH inhibition induces EMT is recapitulated in patient-derived tumors, but with inter-individual differences in responses. Future studies will provide a more detailed and clearer understanding of the wiring of the paracrine HH-FGFR1/tumor-stromal signaling circuit, revealed by the findings reported here, as well as mechanisms of action of this dual-hit combination.

We performed differential, species-deconvolved RNA-Seq analysis of the human (tumor cell) and murine (stromal) compartments of SHHi-treated PDAC PDX tumors to investigate this re-wired paracrine signaling network. Our analysis showed that tumor-derived FGFRs, particularly FGFR1, represented the tyrosine kinase receptor class most upregulated by SHHi treatment. Upstream master-regulator- and kinase enrichment analyses also identified FGFR1, along with Erk1/2, as the most up-regulated candidates. Whereas tumor FGFRs were upregulated by SHHi treatment, tumor-derived FGF was downregulated and stroma-derived FGF expression doubled, establishing that SHHi responses are cell-type specific, paracrine in nature, and that tumor compartment responses are influenced by stroma.

FGFR1 activation can promote EMT by several mechanisms that are well-established in the literature. Canonical FGFR1 signaling mechanisms transcriptionally-activate EMT genes *via* Erk1/2-activation and promote cell migration(17,18,32). Additionally, activation of integrative nuclear FGFR1 signaling, in which endoplasmic FGFR1 is redirected toward the nucleus (nuFGFR1) rather than to the plasma membrane, can drive phenotypic transitions *via* direct promoter binding and gene transcription(34). In SHHi-treated tumors, nuFGFR1 predominated in EMT-polarized, mesenchymal tumor cells, whereas proliferating tumor cells displayed cytoplasmic FGFR1. Sequential SHHi+FGFRi depleted nuFGFR1 and restored cytoplasmic FGFR1, paralleling restoration of a more epithelioid phenotype, and consistent with reports showing FGFR kinase inhibitors can target and mitigate INFS(36,51). For hypothesis generation, we interrogated human neuronal progenitor cell ChIP-Seq data to identify potential nuFGFR1 targets, given that INFS is well-established and functional in that model(25,26) and the likelihood that numerous processes within pluripotent stem cells are generalizable to other human cell types. Our differential RNA-Seq data showed altered expression of several potential nuFGFR1 targets(25,52-55) in SHHi-treated cells, including ERK1 and pluripotency pathways, that could contribute to FGF-mediated responses to HH signaling interdiction.

In breast cancer, FGFR1 promotes transcription of genes involved in EMT and therapeutic resistance *via* a nuclear pathway, and FGFRi-mediated reduction in nuFGFR1 reduces both EMT and chemo-resistance markers(28,30,31). Here, FGFRi treatment reversed hallmarks of EMT, and caused a drastic decline in poorly-differentiated- and non-proliferative mesenchymal tumor cells. Single-agent FGFRi was effective in decreasing both tumor cells and EMT markers in more poorly-differentiated, mesenchymal PDAC tumors, whereas its effects upon well-differentiated PDAC PDX isolates were less discernable. These observations suggest FGFR1

signaling as an intrinsic participant in the cellular signaling that drives PDAC tumor cell de-differentiation and progression to a more mesenchymal phenotype. Also, given similarities in the fibrotic and epithelioid nature of breast cancer and PDAC, the results also implicate a nuFGFR1 role in detrimental SHHi-induced tumor responses *via* an underlying collaboration between aberrant rewired HH/FGF pathways. Additional evidence, such as ChIP analysis showing direct chromatin binding of FGFR1 in PDAC PDXs, and genetic ablation of key components within this paracrine signaling network, will be required to understand fully the HH/FGFR1 signaling axis and the potential role of nuFGFR1 in driving EMT responses. Nonetheless, data demonstrating that pharmacological inhibition of HH signaling promotes FGFR1 expression and drives EMT, and that inhibition of FGFR signaling by FGFRi reverses deleterious EMT-related SHHi-responses, provide a solid experimental foundation for this hypothesized relationship.

In conclusion, the dual-hit strategy described here appears superior to previous efforts employing chronic, single-agent SHHi exposure to breach the PDAC drug delivery barrier and improve the accessibility of the PDAC tumor interstitium to therapeutic agents. We established previously a direct relationship between increased deposition of antibodies or drug-containing nanoparticles and suppression of PDAC tumor progression, and provided evidence for onset of pharmacodynamic tolerance that abrogates SHHi-mediated tumor priming(6,7). Here we provide evidence that sustained inhibition of HH signaling additionally drives tumors toward EMT, and that by interdicting a novel HH/FGFR signaling axis, sequential FGFRi treatment reverses deleterious effects of SHHi priming while extending the tumor priming window. This dual-hit approach, maximizing the opportunity for long-circulating macromolecular agents such as antibodies and nanoparticle drug carriers to extravasate in PDAC tumors, holds considerable promise to advance PDAC tumor priming, and supports the broader potential of FGFRi in

countering intrinsic EMT drive, and EMT elicited by chemotherapy regimens ((41), unpublished data). Our observation that noninvasive measurement of tumor ADC by DW-MRI correlates with increased tumor permeability/perfusion provides a clinically-deployable tool to assist in clinical translation and optimization of not only SHHi-mediated tumor priming, but other priming strategies as well, and can identify those PDAC patents whose tumors respond to tumor priming approaches. Clearly, SHHi-mediated reduction in fibrosis, enhancement of tumor vascular patency, and promotion of EMT could encourage tumor cell migration, particularly with chronic SHHi treatment. However, the intermittent, sequential dual-hit SHHi+FGFRi treatment strategy proposed has potential to improve drug, antibody, and nanoparticle delivery to PDAC tumors, while countering potential detrimental effects of HH inhibition, thereby improving therapy of this highly fatal cancer.

Acknowledgements

Novartis International AG provided NVP-BGJ398. We thank Dr. W. Sigurdson of the UB Jacobs School of Medicine and Biomedical Sciences Confocal Microscopy and Flow Cytometry Facility for his advice and assistance We thank C. Minx and N.L. Straubinger for technical assistance. The following agencies and grants provided financial support for the work: NIH/NCI grants R21CA234775 (RMS), R21CA168454 (RMS and WWM), R01CA198096, funded under the US-Ireland R&D Partnership program (RMS, WWM, MC, and CJS), NIH/NCATS award UL1TR001412 to the University at Buffalo, the UB/SUNY Center for Protein Therapeutics consortium (RMS), New York State Department of Health NYSTEM grants C026415, C026714, National Science Foundation grants CBET-1555720 and CBET-1706050) (MKS and EKS), a Comprehensive Cancer Center Support grant (NIH/NCI P30CA016056) to Roswell Park Comprehensive Cancer Center supported our use of the Translational Imaging, Laboratory Animal, and Gene Modulation Shared Resource cores. Additional support includes US-Ireland R&D Partnership program grant (SFI/14/US/B2997) awarded by Science Foundation Ireland to MC, a US-Ireland R&D Partnership program grant awarded by HSCNI (STL/5010/14) (CJS), MRC grant MC_PC_15013 (CJS and MKG), and CRUK grant C11884/A24367 (SSM). The Genomics Core Technology Unit of the Faculty of Medicine, Health and Life Science, Queen's University Belfast provided RNA-Seq data and analysis.

Author Contributions

Conceptualization	RMS, TR
Experimentation	TR
Data acquisition	TR, QL, SSM
Methodology	TR, JAS, SSM
Software	TR, JAS, SRR, GPQ, SSM
Validation	TR, EKS
Formal Analysis	TR, SRR, GPQ
Investigation	TR, QL, MKG
Resources	RMS, JAS, SSM, CJS, MC, WWM
Writing – Original Draft	TR
Writing – Review, Critical Commenting, Editing	All authors
Visualization	TR, SRR, QL
Supervision	EKS, MKS, SSM, TR, RMS
Funding Acquisition	RMS, WWM, CJS, MC, MKS

References

1. Siegel RL, Miller KD, Jemal A. Cancer statistics, 2019. *CA Cancer J Clin* **2019**;69:7-34.

2. Fiore M, Ramella S, Valeri S, Caputo D, Floreno B, Trecca P, et al. Phase II study of induction chemotherapy followed by chemoradiotherapy in patients with borderline resectable and unresectable locally advanced pancreatic cancer. *Sci Rep* **2017**;7:Art. 45845.

3. Olive KP, Jacobetz MA, Davidson CJ, Gopinathan A, McIntyre D, Honess D, et al. Inhibition of Hedgehog signaling enhances delivery of chemotherapy in a mouse model of pancreatic cancer. *Science* **2009**;324:1457-61.

4. Theunissen JW, de Sauvage FJ. Paracrine Hedgehog signaling in cancer. *Cancer Res* **2009**;69:6007-10.

5. Bailey JM, Swanson BJ, Hamada T, Eggers JP, Singh PK, Caffery T, et al. Sonic hedgehog promotes desmoplasia in pancreatic cancer. *Clin Cancer Res* **2008**;14:5995-6004.

6. Roy Chaudhuri T, Straubinger NL, Pitoniak RF, Hylander BL, Repasky EA, Ma WW, Straubinger RM. Tumor-priming Smoothened inhibitor enhances deposition and efficacy of cytotoxic nanoparticles in a pancreatic cancer model. *Mol Cancer Ther* **2016**;15:84-93.

7. Wang J, Chan DK, Sen A, Ma WW, Straubinger RM. Tumor priming by SMO inhibition enhances antibody delivery and efficacy in a pancreatic ductal adenocarcinoma model. *Mol Cancer Ther* **2019**;18:2074-84.

8. Catenacci DV, Junttila MR, Karrison T, Bahary N, Horiba MN, Nattam SR, et al. Randomized phase Ib/II study of gemcitabine plus placebo or vismodegib, a Hedgehog

pathway inhibitor, in patients with metastatic pancreatic cancer. *J Clin Oncol* **2015**;33:4284-92.

9. Ko AH, LoConte N, Tempero MA, Walker EJ, Kate Kelley R, Lewis S, et al. A Phase I study of FOLFIRINOX plus IPI-926, a hedgehog pathway inhibitor, for advanced pancreatic adenocarcinoma. *Pancreas* **2016**;45:370-5.

10. Lee JJ, Perera RM, Wang H, Wu DC, Liu XS, Han S, et al. Stromal response to Hedgehog signaling restrains pancreatic cancer progression. *Proc Natl Acad Sci USA* **2014**;111:E3091-100.

11. Rhim AD, Oberstein PE, Thomas DH, Mirek ET, Palermo CF, Sastra SA, et al. Stromal elements act to restrain, rather than support, pancreatic ductal adenocarcinoma. *Cancer Cell* **2014**;25:735-47.

12. Ozdemir BC, Pentcheva-Hoang T, Carstens JL, Zheng X, Wu CC, Simpson TR, et al. Depletion of Carcinoma-Associated Fibroblasts and Fibrosis Induces Immunosuppression and Accelerates Pancreas Cancer with Reduced Survival. *Cancer Cell* **2015**;28:831-3.

13. Steele NG, Biffi G, Kemp SB, Zhang Y, Drouillard D, Syu L, et al. Inhibition of Hedgehog signaling alters fibroblast composition in pancreatic cancer. *Clin Cancer Res* **2021**;27:2023-37.

14. Ho WJ, Jaffee EM, Zheng L. The tumour microenvironment in pancreatic cancer - clinical challenges and opportunities. *Nat Rev Clin Oncol* **2020**;17:527-40.

15. Matsumura Y, Maeda H. A new concept for macromolecular therapeutics in cancer chemotherapy: mechanism of tumoritropic accumulation of proteins and the antitumor agent smancs. *Cancer Res* **1986**;46:6387-92.

16. Roy Chaudhuri T, Arnold RD, Yang J, Turowski SG, Qu Y, Spernyak JA, et al. Mechanisms of tumor vascular priming by a nanoparticulate doxorubicin formulation. *Pharm Res* **2012**;29:3312-24.

17. Nguyen PT, Tsunematsu T, Yanagisawa S, Kudo Y, Miyauchi M, Kamata N, Takata T. The FGFR1 inhibitor PD173074 induces mesenchymal-epithelial transition through the transcription factor AP-1. *Br J Cancer* **2013**;109:2248-58.

18. Qian X, Anzovino A, Kim S, Suyama K, Yao J, Hulit J, et al. N-cadherin/FGFR promotes metastasis through epithelial-to-mesenchymal transition and stem/progenitor cell-like properties. *Oncogene* **2014**;33:3411-21.

19. Brown WS, Tan L, Smith A, Gray NS, Wendt MK. Covalent targeting of fibroblast growth factor receptor inhibits metastatic breast cancer. *Mol Cancer Ther* **2016**;15:2096-106.

20. Carstens JL, Shahi P, Van Tsang S, Smith B, Creighton CJ, Zhang Y, et al. FGFR1-WNT-TGF-beta signaling in prostate cancer mouse models recapitulates human reactive stroma. *Cancer Res* **2014**;74:609-20.

21. Hylander BL, Pitoniak R, Penetrante RB, Gibbs JF, Oktay D, Cheng J, Repasky EA. The anti-tumor effect of Apo2L/TRAIL on patient pancreatic adenocarcinomas grown as xenografts in SCID mice. *J Transl Med* **2005**;3:22.

22. Schindelin J, Arganda-Carreras I, Frise E, Kaynig V, Longair M, Pietzsch T, et al. Fiji: an open-source platform for biological-image analysis. *Nat Methods* **2012**;9:676-82.

23. Costes SV, Daelemans D, Cho EH, Dobbin Z, Pavlakis G, Lockett S. Automatic and quantitative measurement of protein-protein colocalization in live cells. *Biophys J* **2004**;86:3993-4003.

24. Yu G, Wang LG, Han Y, He QY. clusterProfiler: an R package for comparing biological themes among gene clusters. *OMICS* **2012**;16:284-7.

25. Narla ST, Lee YW, Benson CA, Sarder P, Brennand KJ, Stachowiak EK, Stachowiak MK. Common developmental genome deprogramming in schizophrenia - Role of Integrative Nuclear FGFR1 Signaling (INFS). *Schizophr Res* **2017**;185:17-32.

26. Drummond DC, Noble CO, Guo Z, Hong K, Park JW, Kirpotin DB. Development of a highly active nanoliposomal irinotecan using a novel intraliposomal stabilization strategy. *Cancer Res* **2006**;66:3271-7.

27. Wang W, Wyckoff JB, Frohlich VC, Oleynikov Y, Huttelmaier S, Zavadil J, et al. Single cell behavior in metastatic primary mammary tumors correlated with gene expression patterns revealed by molecular profiling. *Cancer Res* **2002**;62:6278-88.

28. Kurosawa J, Tawada K, Mikata R, Ishihara T, Tsuyuguchi T, Saito M, et al. Prognostic relevance of apparent diffusion coefficient obtained by diffusion-weighted MRI in pancreatic cancer. *J Magn Reson Imaging* **2015**;42:1532-7.

29. Heid I, Steiger K, Trajkovic-Arsic M, Settles M, Esswein MR, Erkan M, et al. Co-clinical assessment of tumor cellularity in pancreatic cancer. *Clin Cancer Res* **2016**;23:1461-70.

30. Tape CJ, Ling S, Dimitriadi M, McMahon KM, Worboys JD, Leong HS, et al. Oncogenic KRAS Regulates Tumor Cell Signaling via Stromal Reciprocation. *Cell* **2016**;165:910-20.

31. Olea-Flores M, Zuniga-Eulogio MD, Mendoza-Catalan MA, Rodriguez-Ruiz HA, Castaneda-Saucedo E, Ortuno-Pineda C, et al. Extracellular-signal regulated kinase: a central molecule driving epithelial-mesenchymal transition in cancer. *Int J Mol Sci* **2019**;20.

32. Lamouille S, Xu J, Derynck R. Molecular mechanisms of epithelial-mesenchymal transition. *Nat Rev Mol Cell Biol* **2014**;15:178-96.

33. Strutz F, Zeisberg M, Ziyadeh FN, Yang CQ, Kalluri R, Muller GA, Neilson EG. Role of basic fibroblast growth factor-2 in epithelial-mesenchymal transformation. *Kidney Int* **2002**;61:1714-28.

34. Formisano L, Stauffer KM, Young CD, Bhola NE, Guerrero-Zotano AL, Jansen VM, et al. Association of FGFR1 with ER-a maintains ligand-independent er transcription and mediates resistance to estrogen deprivation in ER(+) breast cancer. *Clin Cancer Res* **2017**;23:6138-50.

35. Servetto A, Kollipara R, Formisano L, Lin CC, Lee KM, Sudhan DR, et al. Nuclear FGFR1 regulates gene transcription and promotes antiestrogen resistance in ER(+) breast cancer. *Clin Cancer Res* **2021**;27:4379-96.

36. Chioni AM, Grose R. FGFR1 cleavage and nuclear translocation regulates breast cancer cell behavior. *J Cell Biol* **2012**;197:801-17.

37. Fang X, Stachowiak EK, Dunham-Ems SM, Klejbor I, Stachowiak MK. Control of CREB-binding protein signaling by nuclear fibroblast growth factor receptor-1: a novel mechanism of gene regulation. *J Biol Chem* **2005**;280:28451-62.

38. Coleman SJ, Chioni AM, Ghallab M, Anderson RK, Lemoine NR, Kocher HM, Grose RP. Nuclear translocation of FGFR1 and FGF2 in pancreatic stellate cells facilitates pancreatic cancer cell invasion. *EMBO Mol Med* **2014**;6:467-81.

39. Guagnano V, Kauffmann A, Wohrle S, Stamm C, Ito M, Barys L, et al. FGFR genetic alterations predict for sensitivity to NVP-BGJ398, a selective pan-FGFR inhibitor. *Cancer Discov* **2012**;2:1118-33.

40. Guagnano V, Furet P, Spanka C, Bordas V, Le Douget M, Stamm C, et al. Discovery of 3-(2,6-dichloro-3,5-dimethoxy-phenyl)-1-{6-[4-(4-ethyl-piperazin-1-yl)-phenylamin o]-pyrimidin-4-yl}-1-methyl-urea (NVP-BGJ398), a potent and selective inhibitor of the fibroblast growth factor receptor family of receptor tyrosine kinase. *J Med Chem* **2011**;54:7066-83.

41. Lin Q, Serratore A, Perri J, Roy Chaudhuri T, Qu J, Ma WW, et al. FGFR1 expression correlates inversely with the efficacy of single-agent FGFR-specific inhibitors in pancreatic cancer. *Br J Pharmacol* **2023**;In Press:doi 10.1111/bph.16289.

42. Erkan M, Reiser-Erkan C, Michalski CW, Deucker S, Sauliunaite D, Streit S, et al. Cancer-stellate cell interactions perpetuate the hypoxia-fibrosis cycle in pancreatic ductal adenocarcinoma. *Neoplasia* **2009**;11:497-508.

43. Komar G, Kauhanen S, Liukko K, Seppanen M, Kajander S, Ovaska J, et al. Decreased blood flow with increased metabolic activity: a novel sign of pancreatic tumor aggressiveness. *Clin Cancer Res* **2009**;15:5511-7.

44. Chauhan VP, Martin JD, Liu H, Lacorre DA, Jain SR, Kozin SV, et al. Angiotensin inhibition enhances drug delivery and potentiates chemotherapy by decompressing tumour blood vessels. *Nat Commun* **2013**;4:2516.

45. Provenzano PP, Cuevas C, Chang AE, Goel VK, Von Hoff DD, Hingorani SR. Enzymatic targeting of the stroma ablates physical barriers to treatment of pancreatic ductal adenocarcinoma. *Cancer Cell* **2012**;21:418-29.

46. Ramanathan RK, McDonough SL, Philip PA, Hingorani SR, Lacy J, Kortmansky JS, et al. Phase IB/II randomized study of FOLFIRINOX plus pegylated recombinant human hyaluronidase versus FOLFIRINOX alone in patients with metastatic pancreatic adenocarcinoma: SWOG S1313. *J Clin Oncol* **2019**;37:1062-9.

47. Murphy JE, Wo JY, Ryan DP, Clark JW, Jiang W, Yeap BY, et al. Total neoadjuvant therapy with FOLFIRINOX in combination with losartan followed by chemoradiotherapy for locally advanced pancreatic cancer: a phase 2 clinical trial. *JAMA Oncol* **2019**;5:1020-7.

48. Kasi A, Allen J, Mehta K, Dandawate P, Saha S, Bossmann S, et al. Association of losartan with outcomes in metastatic pancreatic cancer patients treated with chemotherapy. *J Clin Transl Res* **2021**;7:257-62.

49. Simionato F, Zecchetto C, Merz V, Cavaliere A, Casalino S, Gaule M, et al. A phase II study of liposomal irinotecan with 5-fluorouracil, leucovorin and oxaliplatin in patients with resectable pancreatic cancer: the nITRO trial. *Ther Adv Med Oncol* **2020**;12:1758835920947969.

50. Williams RM, Zipfel WR, Webb WW. Interpreting second-harmonic generation images of collagen I fibrils. *Biophys J* **2005**;88:1377-86.

51. Stachowiak EK, Benson CA, Narla ST, Dimitri A, Chuye LEB, Dhiman S, et al. Cerebral organoids reveal early cortical maldevelopment in schizophrenia-computational anatomy and genomics, role of FGFR1. *Transl Psychiatry* **2017**;7:Art. 6.

52. Lee YW, Terranova C, Birkaya B, Narla S, Kehoe D, Parikh A, et al. A novel nuclear FGF Receptor-1 partnership with retinoid and Nur receptors during developmental gene programming of embryonic stem cells. *J Cell Biochem* **2012**;113:2920-36.

53. Narla ST, Decker B, Sarder P, Stachowiak EK, Stachowiak MK. Induced pluripotent stem cells reveal common neurodevelopmental genome deprograming in schizophrenia. *Results Probl Cell Differ* **2018**;66:137-62.

54. Terranova C, Narla ST, Lee YW, Bard J, Parikh A, Stachowiak EK, et al. Global developmental gene programing involves a nuclear form of fibroblast growth factor receptor-1 (FGFR1). *PLoS One* **2015**;10:e0123380.

55. Stachowiak MK, Birkaya B, Aletta JM, Narla ST, Benson CA, Decker B, Stachowiak EK. Nuclear FGF receptor-1 and CREB binding protein: an integrative signaling module. *J Cell Physiol* **2015**;230:989-1002.

Figure Legends

Fig. 1. SHHi increases tumor ADC and permeability.

(A) *Sc* PDX #18254 showed 20-fold lower Gd-DTPA contrast enhancement than orthotopic glioblastoma (GL261). **(B)** SHHi-responsive PDX #18269 (*Supp Fig. S2A-C*) did not show contrast enhancement with albumin-bound-Gd (HSA-Gd) on d1, d5, and d9 of treatment. **(C,D)** ADC map overlaid upon anatomical images of PDX #14312 on d0, 3, 7 of SHHi treatment (N=3 mice/time point) with 25% sucrose internal standard. **(C)** Controls showed consistently low ADC, whereas **(D)** SHHi treatment increased ADC. Relative ADC (normalized to pretreatment values) was elevated significantly by daily SHHi treatment of PDXs **(E)** #18269 (d3: * $p<0.05$; d7: ** $p<0.01$) and **(F)** #14312 (d3: * $p<0.05$), but was not changed significantly in **(G)** #18254. **(H-J)** Tumor deposition of *iv* 80nm SSL-DiI correlated linearly with absolute ADC of individual tumors. Dashed curves: 5^{th}, 95^{th} percentile range of data. (**K-N**) Tumor volume progression. SHHi pretreatment enhanced SSL-DXR efficacy in priming-responsive #18269 but not priming-refractory #18254. Three cycles of 7d oral SHHi pretreatment were performed, followed by *iv* administration of SSL-DXR (6 mg/kg) on the last day of each cycle, denoted by vertical dashed lines. A 7-day drug holiday followed each treatment cycle (**K,M**). Tumor volume progression was tested statistically on d42 (**L,N**): * $p<0.05$; ** $p<0.01$; *** $p<0.001$.

Fig. 2. ADC alterations parallel tumor morphological changes.

Collagen I (red) or tumor cells (huMITO; green) staining in PDXs **(A)** #18269 and **(B)** #14312. Bar: 200μm. PDX #18269 show abundant collagen I and epithelioid tumor cells; SHHi treatment reorganized glandular structures, significantly decreasing stromal expanses of collagen (**C**; $p<0.01$) and increasing tumor cells . **(B)** PDX #14312 had numerous small glandular structures

and collagen I bands; SHHi treatment decreased collagen I significantly on d4 (**D**; $p<0.01$) and enhanced tumor cell regions. **(E,F)** Decreased collagen I correlated inversely with absolute ADC in individual tumors of both models ($p<0.05$; dashed curves: 5^{th}, 95^{th} percentiles). **(G)** SHHi treatment did not alter overall nuclear density in PDX #18269, but **(H,I)** increased the area occupied by tumor cells 1.5-fold after 4d or 8d of SHHi treatment in both PDXs (** $p<0.01$). **(J,K)** Collagen I decrease and tumor cell enhancement showed reciprocal relationship in both PDXs.

Fig. 3. FGFR1 translocates to nuclei in EMT-polarized cells.

Confocal 2μm z-stacks of control and SHHi-treated PDX #18269 (n=3) stained with green human-specific vimentin or Ki67, FGFR1 extracellular domain (red), and nuclei (blue). **(A)** Controls had few vimentin$^+$ tumor cells, but **(B)** SHHi induced larger clusters; bar: 50μm. Magnified inset reveal nuclear FGFR1 localization (speckled pattern) in vimentin$^+$ tumor cells; bar: 5μm. **(C)** Ki67$^+$ tumor cells (green) were infrequent in controls but **(D)** increased with SHHi-treatment; bar: 25μm. Magnified inset show that Ki67$^+$ tumor cells in both groups lacked nuFGFR1; bar: 5μm. The SHHi treatment- **(E)** increased vimentin$^+$ cells 3-fold (*** $p<0.001$), **(F)** increased Ki67$^+$ cells 2-fold compared to control, **(G)** enriched GSEA clusters of EMT, inflammation (IL2_STAT5), cell cycle deregulation and stress responses by RNA-Seq, **(H)** upregulated IFNγR heterodimers (* $p<0.05$), and **(I)** stemness transcription factors Oct4 and NANOG (*; $p<0.05$). **(J-L)** Heatmap comparing gene expression data of vehicle- (purple) *vs.* SHHi-treated (green) groups for GSEA clusters EMT, IL2_STAT5, and G2M checkpoint.

Fig. 4. SHHi treatment increases FGFR1 signaling in tumors.

Control and SHHi-treated PDX #18269 were stained for p-Erk1/2 or FGFR1 (red), tumor cells (huMITO; green), and nuclei (DAPI; blue). Exposure settings were kept constant among groups. **(A,B)** p-Erk1/2 expression was higher in the abundant tumor cells induced by SHHi. The SHHi-**(C)** upregulated ERK1 than controls (** $p<0.01$), whereas ERK2 and MEK 1/2 remained unchanged, **(D)** upregulated tumor-derived FGFR1 and FGFR3, but downregulated FGFR2 ($p<0.01$), and **(E)** downregulated tumor-derived FGF2 ligand (* $p<0.05$), but **(F)** upregulated stromal (murine) FGF1 ligand (*), suggesting a significant stromal contribution to FGF ligand production. High-resolution confocal z-stacks (2µm) show **(G)** FGFR1 (red) within epithelioid tumor cells of controls, **(H)** which increased in magnitude and distribution in SHHi-treated tumors; bar: 50µm. **(I-top, bottom)** Controls show a small proportion of cells with nuclear FGFR1 (bars: 10 µm, 5µm). **(J-top)** SHHi-treatment increased FGFR1 expression in **(left)** gland-associated tumor cell clusters and **(right)** stroma-embedded spindle-shaped tumor cells (bars: 10µm), where **(bottom)** FGFR1 colocalized with the nuclei (arrows; bars: 5µm). **(K)** Quantification of FGFR1/nuFGFR1: SHHi **(left)** significantly increased total tumor-derived FGFR1 (* $p<0.05$), **(middle panel)** doubled tumor-derived nuFGFR1 (colocalized $FGFR1^{+}/DAPI^{+}$ pixels) (** $p<0.01$), **(right panel)** but not stroma-derived nuFGFR1. **(L)** UCSC genome browser visualization of FGFR1 binding peak distribution on the MAPK3 (Erk1) promoter, mined from ChIP-seq analysis of human neuronal progenitor cell chromatin sequences pulled down by anti-human FGFR1 (25).

Fig. 5. Dual-hit priming reverses EMT and restores differentiated tumor features.

Controls and PDX #18269 treated with SHHi, FGFRi and SHHi/FGFRi sequence were stained and image features and marker expression were quantified. **(A)** huMITO (tumor cells, green) and

collagen I (red) staining showed drastic reorganization of glandular structures with 7d and 10d SHHi treatment, and FGFRi restored control-like architecture. Bar: 200μm. **(B)** Bars indicate group comparisons, symbols indicate significance: * $p<0.05$; ** $p<0.01$; *** $p<0.001$: SHHi-treatment significantly increased the number of tumor cells compared to controls on d8 and d11, which was significantly reduced by sequential SHHi+FGFRi. Whereas SHHi-treatment reduced collagen I significantly, it was restored to control levels by SHHi+FGFRi. The FGFRi reduced tumor cells significantly. Tumor sections were also co-stained for FGFR1 (red) and **(C)** vimentin (green) or **(D)** Ki67 (green) (Bar: 50μm); **(E)** SHHi treatment increased overall FGFR1 expression, doubled the proportion of nuFGFR1$^+$ tumor cells, tripled vimentin$^+$ tumor cells and doubled proliferating (Ki67$^+$) cells. With sequential SHHi+FGFRi treatment, FGFR1 expression remained high, but vimentin$^+$ and nuFGFR1$^+$ cells reverted to control levels, and Ki67$^+$ cells were slightly but significantly reduced. FGFRi did not mitigate vimentin$^+$ or Ki67$^+$ numbers, but reduced nuFGFR1$^+$ cells significantly. Bar: 50μm. **(F-G)** Western blot (β-actin normalization) showed SHHi-treatment doubled Erk1/2 and p-Erk1/2, and the sequence restored them to control levels; SHHi did not increase p-Mek1/2 or Mek1/2 significantly; the sequence had an inhibitory effect on Mek1/2, but it increased p-Mek1/2 significantly.

Fig. 6. Dual-hit priming enhances functional vasculature and nanoparticle delivery.

Tumor-bearing mice treated daily with vehicle, SHHi, FGFRi, or SHHi+FGFRi. SSL-DiI were administered *as* permeability probes and lectin-FITC to label functional vessels, 24hr and 10 min before sacrifice respectively. Significance of comparisons: * $p<0.05$; ** $p<0.01$; *** $p<0.001$. **(A)** Functional vessels and **(B)** SSL-DiI deposition representative images. Functional vessel morphology, density and SSL-DiI were quantified. **(C)** Perfused area, **(D)** average vessel size, and **(E)** density of functional vessels increased over 7d SHHi, but 10d SHHi reverted perfused-

area and vessel-size to control values, although functional vascular density remained elevated. Sequential SHHi+FGFRi sustained vascular patency, perfusion and functional vessel size through d11, and increased functional vessel density further (*). **(F)** SSL-DiI deposition doubled after 8d and waned by d11 of SHHi treatment; sequential SHHi-FGFRi prevented this tolerance, and maintained vascular permeability and SSL-DiI delivery. **(G)** Relative ADC quantified by DW-MRI increased significantly by d3 (*) but declined by d10 of SHHi treatment. Sequential SHHi+FGFRi significantly elevated relative ADC **(H)** compared vehicle (**), SHHi alone (*), or 3d of FGFRi alone (*). **(I)** Absolute ADC values correlated linearly with nanoparticle deposition in each individual animal of all groups. FGFRi alone had no apparent vascular effect in PDX#18269.

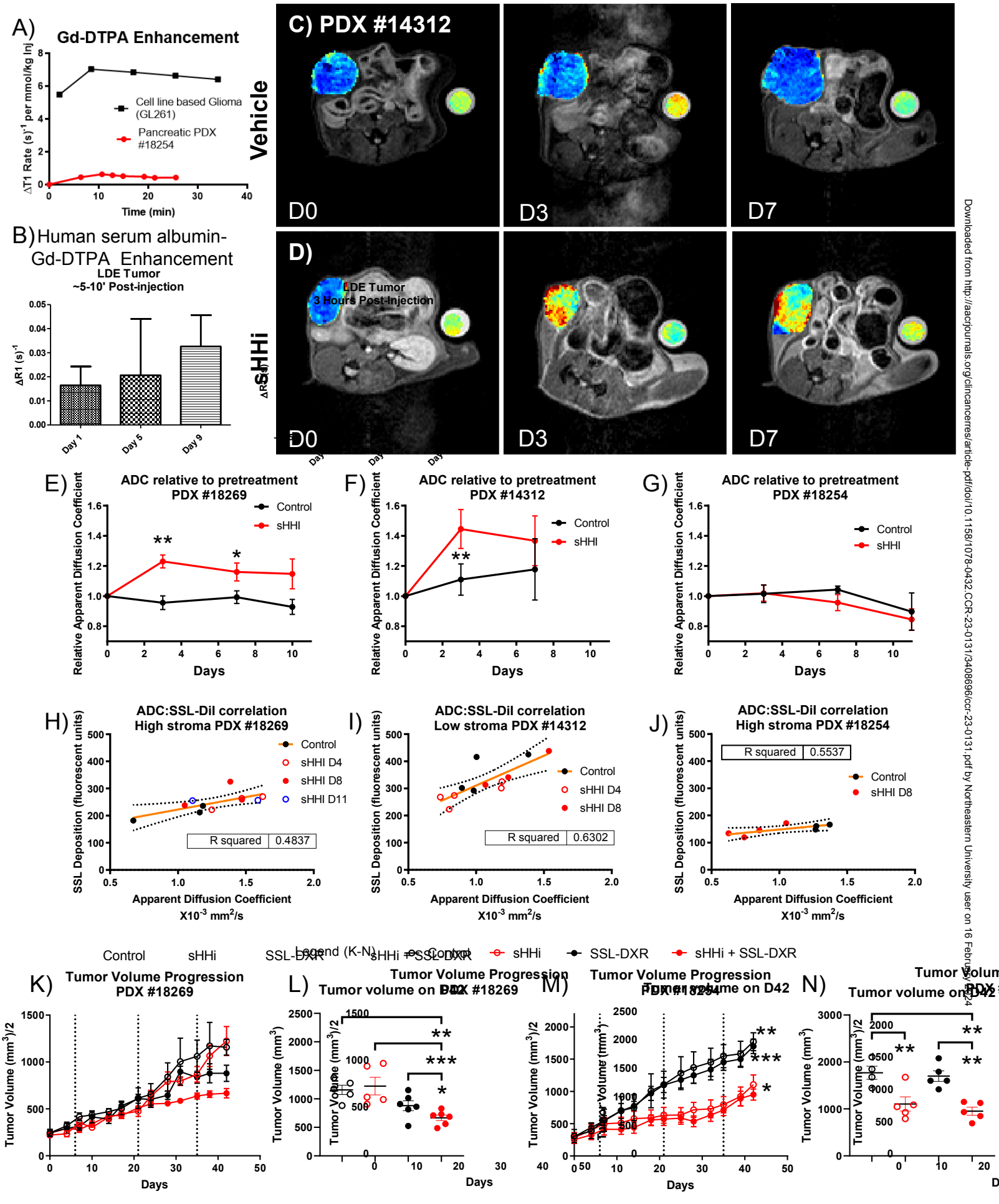

Figure 2

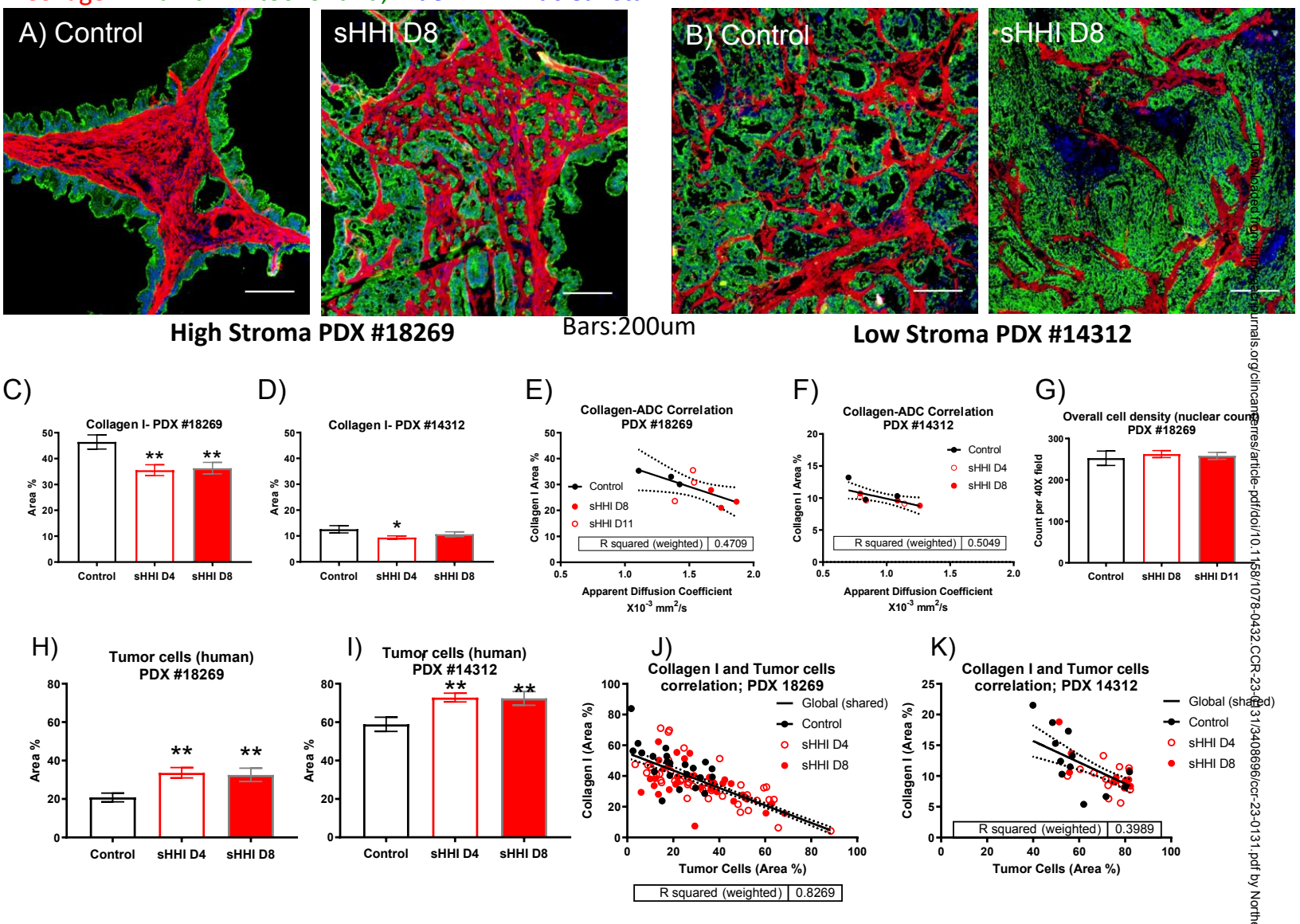

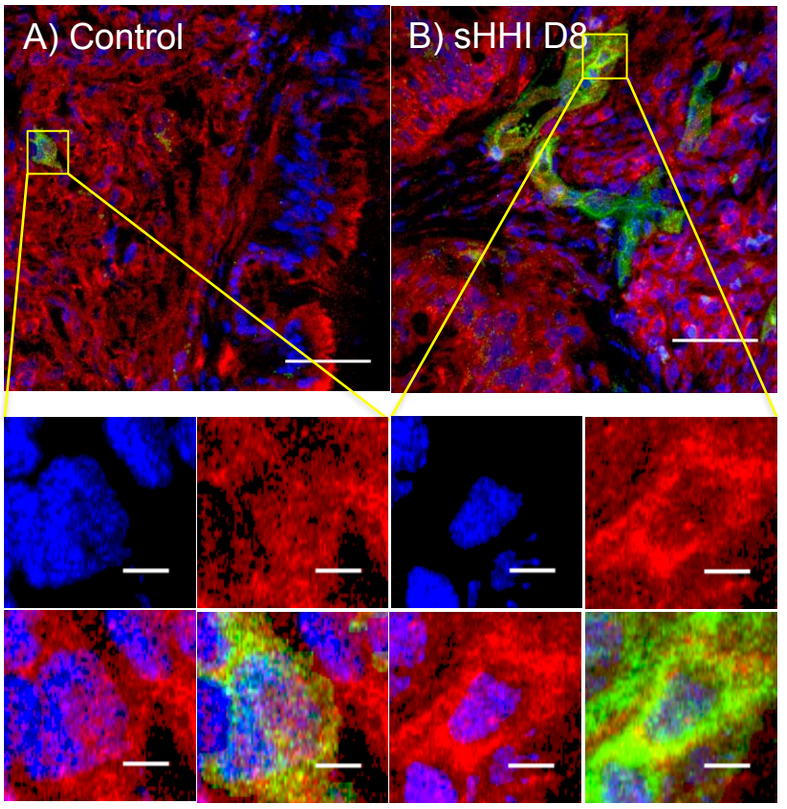

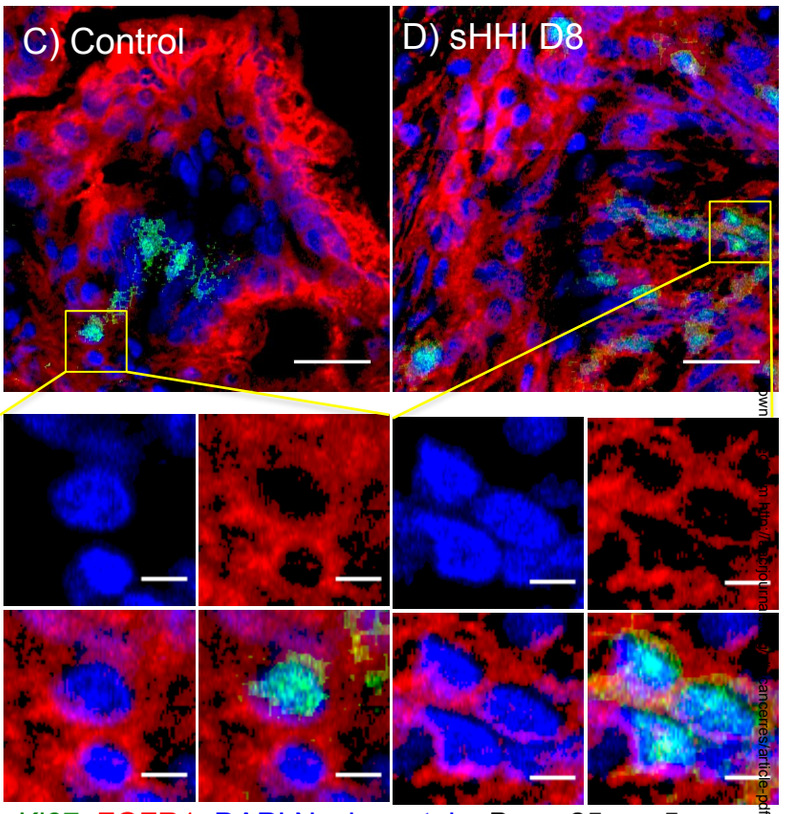

Top: Vimentin; FGFR1; DAPI Nuclear stain Bars: 50um, 5um

Ki67; FGFR1; DAPI Nuclear stain. Bars: 25um, 5um

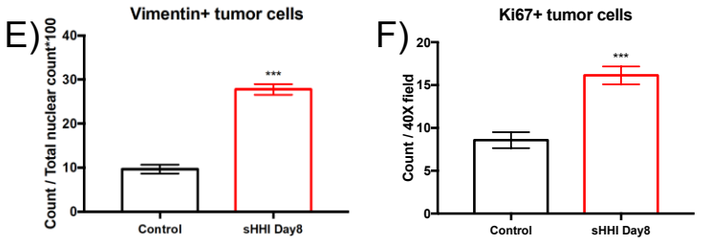

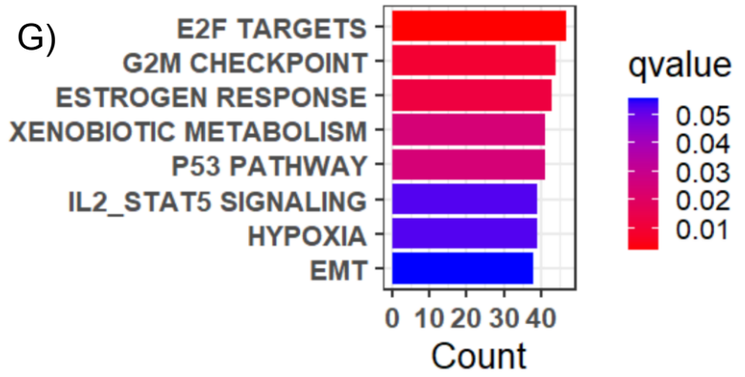

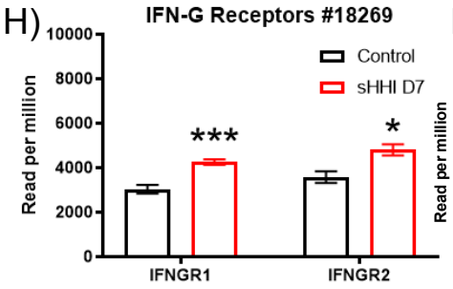

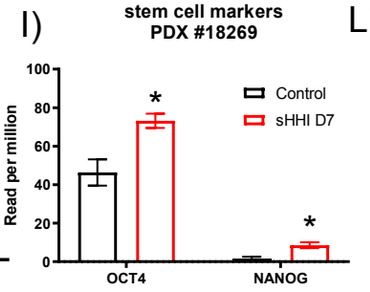

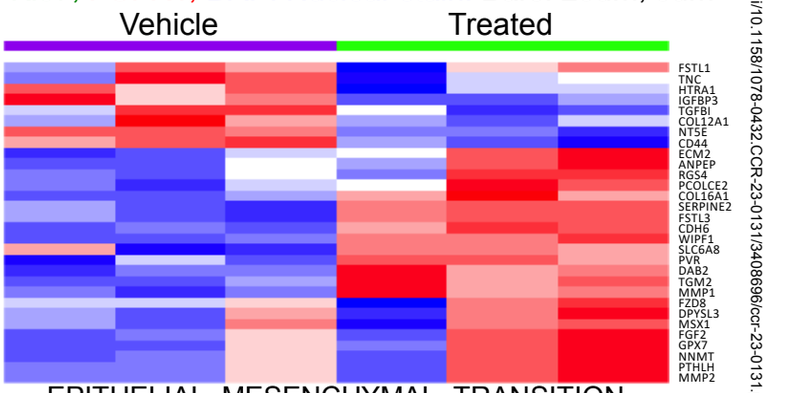

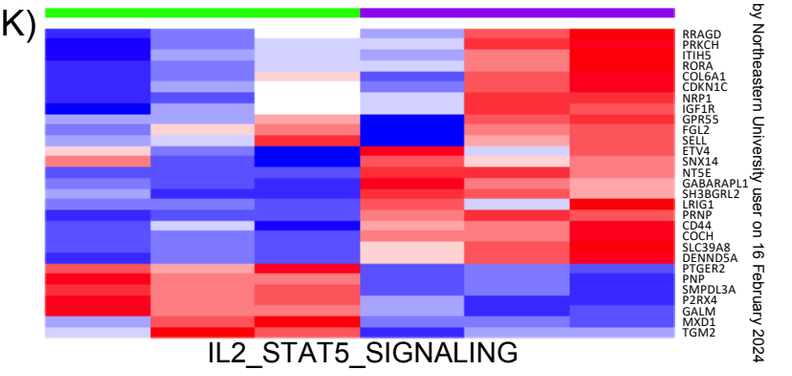

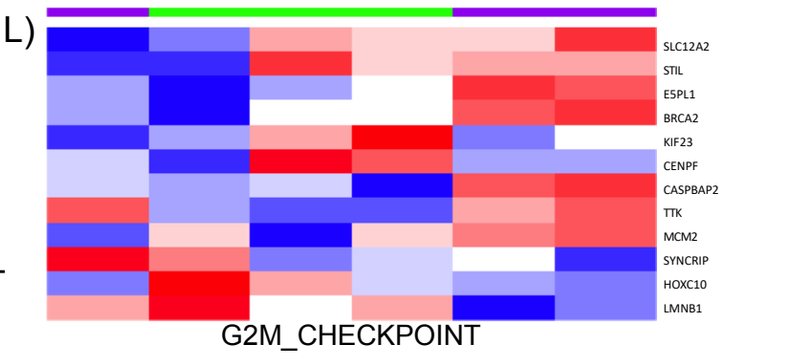

Figure 4

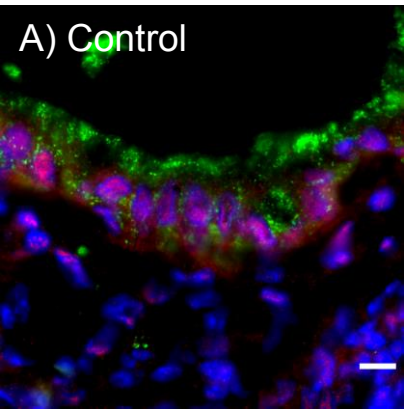

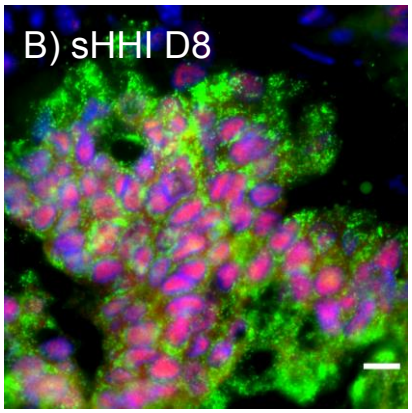

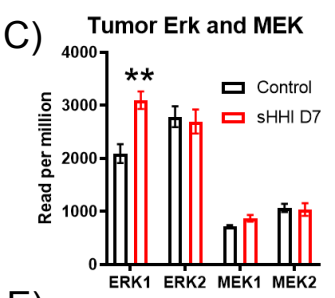

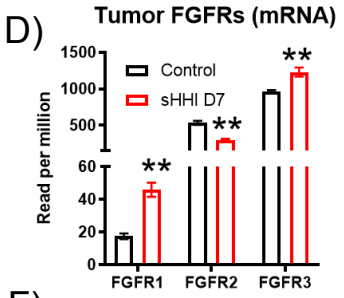

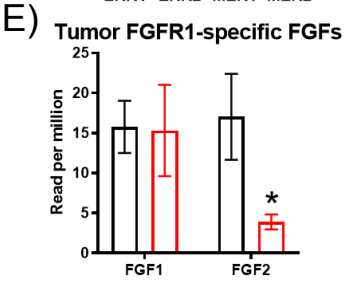

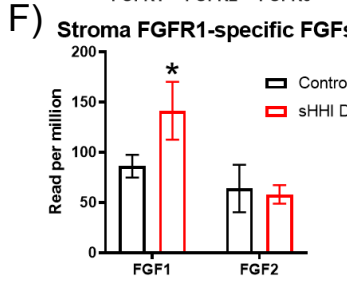

Above: Red=p-Erk1/2;
Below: Red=FGFR1; Green= Human mitochondria;
Blue=DAPI+ Nucleus

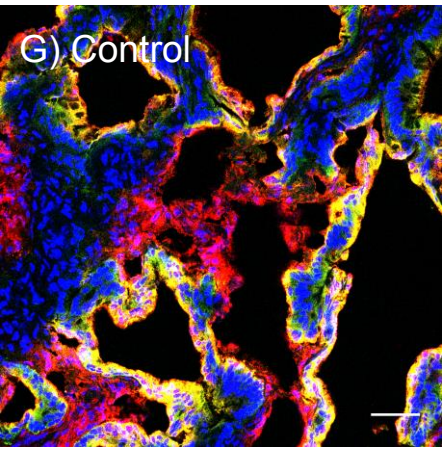

I) Control

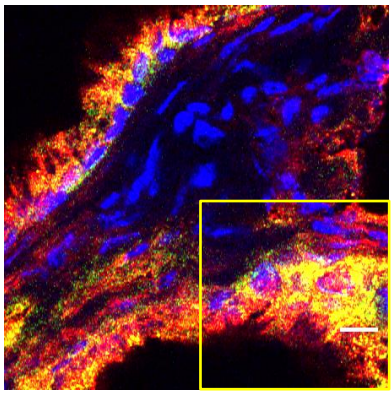

J) sHHi D8

Associated with glands

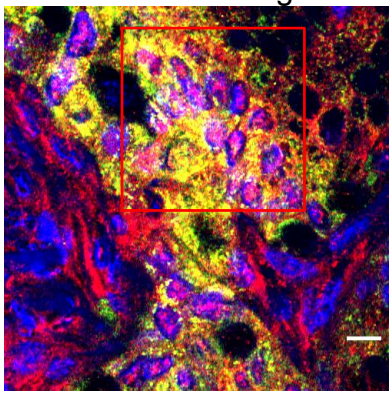

Embedded in stroma

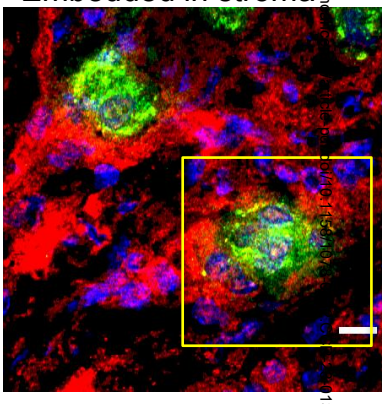

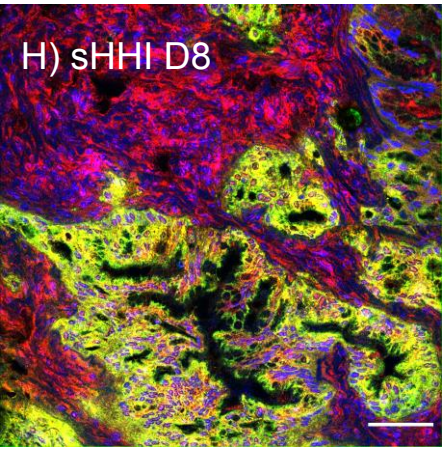

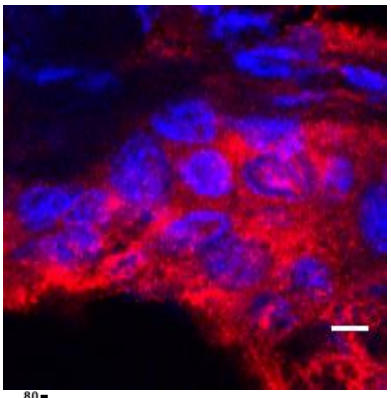

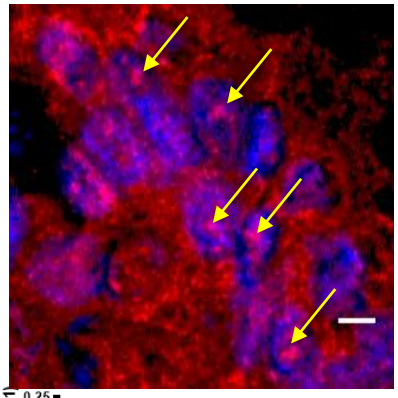

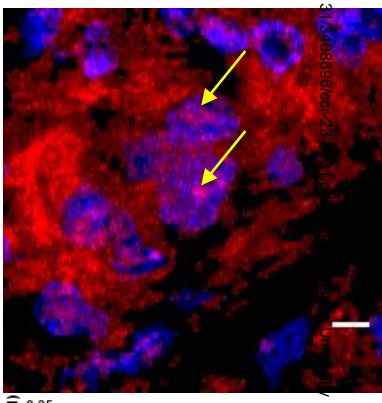

K) FGFR1 quantification

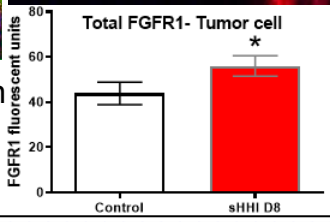

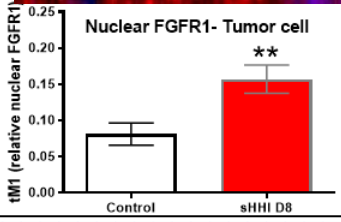

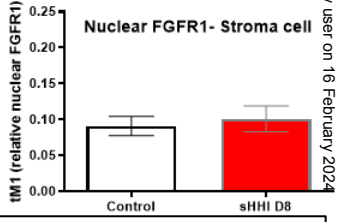

L)

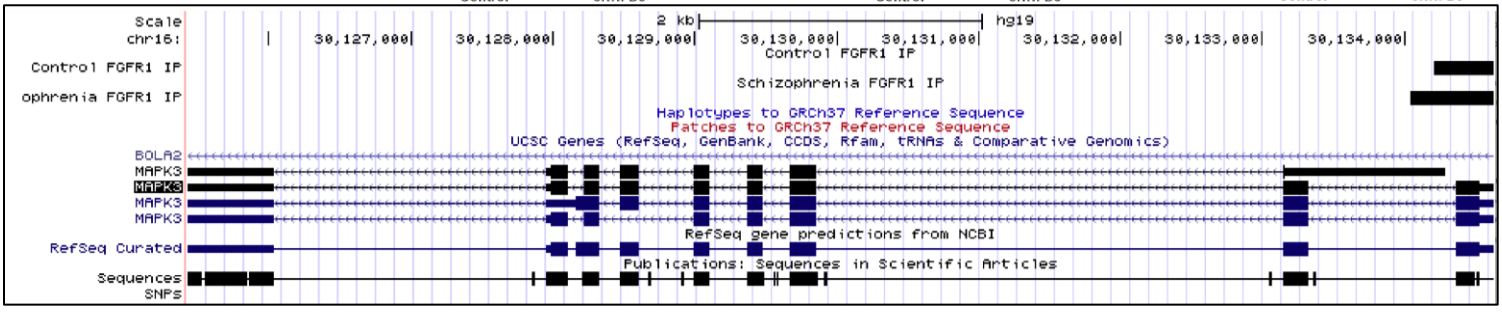

Figure 5

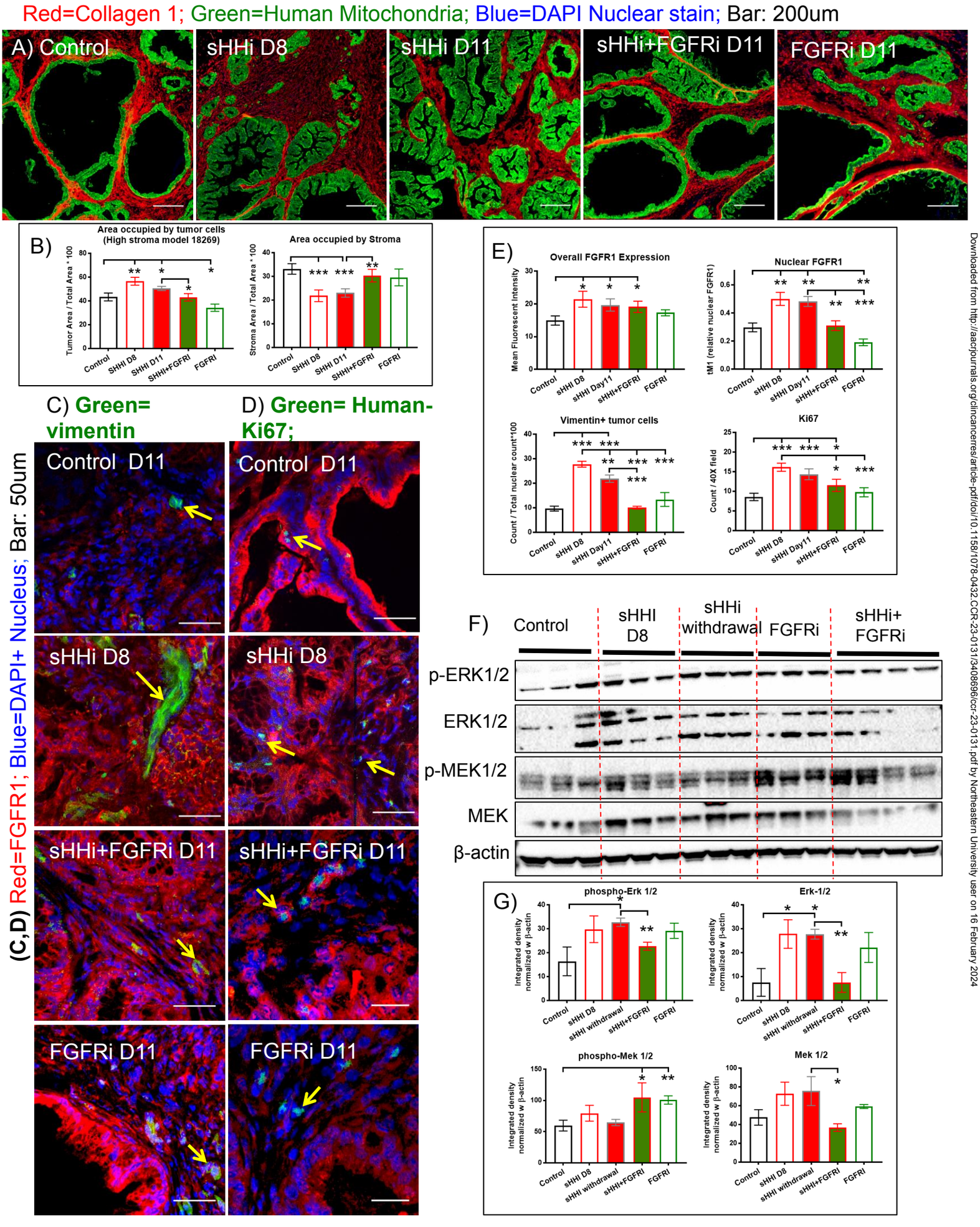

Figure 6

(A) Lectin bound to functional vessels; Bars: 50um **(B)** Red=Fluorescent liposome (SSL)